

External pressure-triggering of star formation in a disc galaxy: a template for positive feedback

Rebekka Bieri^{1*}, Yohan Dubois¹, Joseph Silk^{1,2,3,4}, Gary A. Mamon¹
and Volker Gaibler⁵

¹ Institut d'Astrophysique de Paris (UMR 7095: CNRS & UPMC – Sorbonne Universités), 98 bis bd Arago, F-75014 Paris, France

² Laboratoire AIM-Paris-Saclay, CEA/DSM/IRFU, CNRS, Univ. Paris VII, F-91191 Gif-sur-Yvette, France

³ Department of Physics and Astronomy, The Johns Hopkins University Homewood Campus, Baltimore, MD 21218, USA

⁴ BIPAC, Department of Physics, University of Oxford, Keble Road, Oxford OX1 3RH

⁵ Institut für Theoretische Astrophysik, Universität Heidelberg, Albert-Ueberle-Str 2, D-69120 Heidelberg, Germany

Accepted . Received ; in original form

ABSTRACT

Feedback from active galactic nuclei (AGN) has often been invoked both in simulations and in interpreting observations for regulating star formation and quenching cooling flows in massive galaxies. AGN activity can, however, also over-pressurise the dense star-forming regions of galaxies and thus enhance star formation, leading to a positive feedback effect. To understand this pressurisation better, we investigate the effect of an ambient external pressure on gas fragmentation and triggering of starburst activity by means of hydrodynamical simulations. We find that moderate levels of over-pressurisation of the galaxy boost the global star formation rate of the galaxy by an order of magnitude, turn stable discs unstable, and lead to significant fragmentation of the gas content of the galaxy, similar to what is observed in high redshift galaxies.

Key words: galaxies: formation — galaxies: active — methods: numerical

1 INTRODUCTION

Supermassive black holes are found at the centers of most, if not all, massive galaxies (e.g., Magorrian et al. 1998; Hu 2008; Kormendy et al. 2011). Throughout cosmic history, they are thought to play an important role in regulating the baryonic mass content of massive galaxies through *feedback* from Active Galactic Nuclei (AGN) by releasing a fraction of the rest-mass accreted energy back into the galactic gas and altering the star formation rate (SFR) in the galaxy.

AGN can exert either *negative* or *positive* feedback on their surroundings. The former describes cases where the AGN inhibits star formation by heating and dispersing the gas in the galaxy, while the latter describes the possibility that an AGN may trigger star formation. Negative AGN feedback can operate in *quasar-mode* from radiation at high accretion rates, or *radio-mode* from AGN jets at predominantly low accretion rates (Churazov et al. 2005; Russell et al. 2013). It is still unclear how efficiently AGN feedback delivers energy (through heating, e.g., Silk & Rees 1998) and momentum (through physical pushing, King 2003) to the galaxy's gas and what mode of feedback dominates. Both semi-analytical (e.g., Croton et al. 2006; Bower et al. 2006) and hydrodynamical cosmological simulations (e.g., Di Matteo et al. 2005, 2008; Sijacki et al. 2007; Booth & Schaye 2009; Dubois et al. 2010) have shown

that negative AGN feedback is an important ingredient in the formation and evolution of massive galaxies, in particular in shaping the observed high-end tail of the galaxy mass function, and the low SFRs in massive galaxies. Moreover, observations show that cooling flows in the hot circumgalactic and intracluster media can be suppressed by the energy transferred by AGN jets (Bîrzan et al. 2004; Dunn et al. 2005), again negatively impacting star formation.

Although AGN feedback has been extensively studied in observations and through cosmological simulations, the impact on the host galaxy and the precise mechanism of the communication of the AGN with the galaxy's interstellar medium (ISM) is far from being understood. It is not clear why jet feedback, which is thought to heat cold gas, should have a similar effect on the multi-phase ISM. It has been argued that a jet that propagates through an inhomogeneous ISM may also trigger or enhance star formation in a galaxy (i.e., positive feedback). Begelman & Cioffi (1989) and Rees (1989) proposed that the radio jet activity triggers star formation and might serve as an explanation for the alignment of radio and optical structures in high redshift radio galaxies. Radio jet-induced star formation has also been considered as a source powering luminous starbursts (Silk 2005). Ishibashi & Fabian (2012) provide a theoretical framework linking AGN feedback triggering of star formation in the host galaxy to the oversized evolution of massive galaxies over cosmic time. Furthermore, negative and positive feedback are not necessarily contradictory (Silk 2013; Zubo-

* E-mail: bieri@iap.fr

vas et al. 2013; Zinn et al. 2013; Cresci et al. 2015): AGN activity may both quench and induce star formation in different parts of the host galaxy and on different time-scales.

Observationally, this positive feedback scenario is directly supported by only a few local (Croft et al. 2006; Inskip et al. 2008; Salomé et al. 2015) and high redshift (Dey et al. 1997; Bicknell et al. 2000; Rauch et al. 2013) observations. There are, however, also indirect links between jets and star formation which suggest possible positive feedback from AGN (Klamer et al. 2004; McCarthy et al. 1991; McCarthy 1993; Balmaverde et al. 2008; Podigachoski et al. 2015; Swinbank et al. 2015).

More recently, high resolution hydrodynamical simulations of a jet including a multi-phase ISM have become feasible (Sutherland & Bicknell 2007; Antonuccio-Delogu & Silk 2008, 2010; Wagner & Bicknell 2011; Gaibler et al. 2012). These studies have shown that a clumpy interstellar structure results in a different interaction between the jet and the gas than was assumed from simulations with a homogeneous ISM. It can be generally noted that an inhomogeneous ISM affects not only the jet evolution, but also the morphology of the host galaxy itself. Simulations by Tortora et al. (2009) extended the studies and generalised the simulations of Antonuccio-Delogu & Silk (2008) studying the interaction of a powerful jet in 2D, two-phase ISM. Tortora et al. (2009) have shown that star formation can initially be slightly increased (10–20 per cent) followed by a much stronger quenching (more than 50 per cent) within a time-scale of a few million years. They argue that the rapid decrease of the SFR after its initial enhancement is a consequence of both the high temperatures as well as the reduced cloud mass once the jet cocoon has propagated within the medium. Kelvin-Helmholtz instabilities reduce the mass of the clouds and, assuming a Schmidt-Kennicutt law, thereby reduce the SFR. It should, however, be noted that the 2D approach results in a very different temperature and pressure evolution as compared to a 3D simulation. Wagner & Bicknell (2011) studied the interaction of a relativistic jet interacting with a two-phase ISM at the galaxy’s center with a resolution of one kiloparsec. They found that the transfer of energy and momentum to the ISM may inhibit star formation through the dispersal of gas, but their simulations do not contain a star-formation model. It could be argued, though, that because of the short ($\lesssim 1$ Myr) simulation timescale, the impact of cooling is very weak and they therefore might underestimate the SFR.

Gaibler et al. (2012) simulated a powerful AGN jet within a massive gaseous, clumpy disc (however they neglected gravity). They showed that the jet activity causes a significant change of the SFR by enhancing the formation of stars, with inside-out propagation in the galaxy (see Dugan et al. 2014). Their simulations show the formation of a blast wave in the central region of the disc possibly dominating the early evolution between the jet and the galaxy. The blast wave results in the formation of a cavity in the disc center pushing the gas outwards and compressing the gas within the disc at the cavity boundary, generating rings of compressed gas within the disc. At later times, the ISM of the disc is pressurised by the bow shock enclosing the entire disc. This pressurisation is both due to the ram pressure from the backflow but also the thermal pressure of the cocoon. It is expected that the thermal pressure dominates somewhat as the turbulence is measured to be in the subsonic or transonic regime.

Although the physical understanding of star formation is still limited and debated (Padoan & Nordlund 2011), it can be assumed that a pressurised disc can trigger gravitational instabilities, compress the galaxy’s clouds, and push the densities within the disc

Table 1. Galaxy parameters: scale radius (r_s), gas fraction (f_g), total stellar mass (M_*), and total gas mass in the disc (M_{gas})

Identifier	r_s [kpc]	f_g [%]	M_* [$10^9 M_\odot$]	M_{gas} [$10^9 M_\odot$]
gasLow	3.4	10	8.1	0.9
gasHigh	3.4	50	4.6	4.4

above the critical density for star formation, thus resulting in an increased SFR. This picture is further supported by a few observations of well-resolved star-forming molecular clouds (Keto et al. 2005; Rosolowsky & Blitz 2005) and by detailed simulation of the ISM (e.g. Slyz et al. 2005; Zubovas et al. 2014).

Motivated by the pressurisation of the disc found by Gaibler et al. (2012) in their hydrodynamical simulations of AGN jet feedback, we have investigated the effects of this extra pressure on a galaxy disc, by running hydrodynamical simulations with self-gravity, without AGN jets, but with simple prescriptions for external pressure such as that which may be caused by the jet cocoon. In a first study (Bieri et al. 2015), we simulated disc galaxies of one-tenth the total mass of the Milky Way, varying their initial gas fraction. We found that with a given level of external pressure, the disk fragments into numerous clumps, causing enhanced star formation. In the present article, we study the effects of external pressure in more detail, by considering different geometries and levels of external pressure, as well as studying the effects of supernova feedback and mass resolution.

In Section 2, we describe our suite of hydrodynamical simulations. Our results are presented in Section 3 and summarised in Section 4.

2 SIMULATION SET-UP

2.1 Basic simulation scheme

Our simulations begin with a galaxy made of a disc of gas and stars, a stellar bulge and a dark matter (DM) halo. We allow this galaxy to relax to an equilibrium configuration (with a reasonable disc thickness) over the rotation time of the disc at its half-mass radius. This first phase is performed without gas cooling, or star formation or feedback, in order to evacuate spurious waves emitted from the imperfect equilibrium of the initial conditions. After this first relaxation phase, we turn on the external pressure, gas cooling, star formation, and also feedback from supernovae (SNe), as described below.

The initial condition method introduced by Springel & Hernquist (2005) is used to generate the DM particles with an NFW (Navarro et al. 1997) density profile and a concentration parameter of $c = 10$. The virial velocity of the DM particles is set to be $v_{200} = 70 \text{ km s}^{-1}$, which corresponds to a virial radius of $R_{200} \approx 96 \text{ kpc}$ and a virial mass of $M_{200} \approx 1.1 \times 10^{11} M_\odot$. A Hubble constant of $H_0 = 73 \text{ km s}^{-1} \text{ Mpc}^{-1}$ is assumed. The star particles as well as the gas are distributed in an exponential disc with a scale length of 3.44 kpc and scale height 0.2 kpc, and a spherical, non rotating bulge with a Hernquist profile (Hernquist 1990) of scale radius 0.2 kpc. We use 10^6 DM particles with a mass resolution of $1.23 \times 10^5 M_\odot$ to sample the dark matter halo, and 5.625×10^5 star particles sampling the disc of which 6.25×10^4 star particles are used to sample the bulge. The stellar mass resolution is $1.57 \times 10^4 M_\odot$ for the 10% gas fraction simulation (hereafter, *gasLow*) whereas for the 50% gas fraction simulation (here-

after, *gasHigh*) the mass resolution is $8.73 \times 10^3 M_\odot$. The relevant galaxy parameters are shown in Table 1.

The simulations are run with the RAMSES adaptive mesh refinement code (Teyssier 2002). Particles motions are evolved through the gravitational force with an adaptive particle mesh solver using a cloud-in-cell interpolation, together with the mass contribution of the gas component. The evolution of the gas is followed with a second-order unsplit Godunov scheme. We use the HLLC Riemann solver (Toro et al. 1994) with MinMod total variation diminishing scheme to reconstruct the interpolated variables from their cell-centred values. The box size is 655 kpc with a coarse level of 7, and a maximum level of 14 corresponding to a $\Delta x = 40$ pc minimum cell size for most of the simulations. For convergence studies, we perform a higher resolution run with a spatial resolution of $\Delta x = 10$ pc (maximum level of refinement 16). The refinement is triggered with a quasi-Lagrangian criterion: if the gas mass within a cell is larger than $8 \times 10^7 M_\odot$ or if more than 8 DM particles are within the cell a new refinement level is triggered.

The circumgalactic medium is modelled with a constant hydrogen number density of $n_{\text{CGM}} = 10^{-3} \text{ H cm}^{-3}$. The pressure and temperature profiles outside the disc are calculated assuming spherical hydrostatic equilibrium. For the relaxation phase, the simulations are run for one rotation period of the half-baryonic mass radius (5 kpc), i.e. $\approx 0.5 \text{ Gyr}$.

The simulations include sub-grid models for cooling, star formation, as well as SN feedback in a subset of runs. The cooling mechanism is that described by Sutherland & Dopita (1993), which accounts for H, He, and metal contributions to gas cooling (assuming a solar chemical composition of the various metal elements, but with a varying metallicity of the gas). The disc is initialised with a uniform solar metallicity. No metals are initially placed outside the disc. The boundary of the disc is defined using a geometrical criteria with cylindrical symmetry using the initial disc radius and disc height. Metals are passively advected with gas in the simulation and are modified by individual SNe events with a yield of 0.1, which also distribute the metals throughout and outside the galaxy. In dense and cold regions, gas is turned into star particles following a Schmidt law:

$$\dot{\rho}_* = \epsilon_* \frac{\rho_{\text{gas}}}{t_{\text{ff}}} \quad \text{if } n_{\text{gas}} > n_0, \quad (1)$$

where $\dot{\rho}_*$ is the star formation rate density, ρ_{gas} is the gas mass density, $\epsilon_* = 0.01$ is the star formation efficiency, t_{ff} is the local gas free-fall time, and n_{gas} and $n_0 = 14 \text{ H cm}^{-3}$ for $\Delta x = 40$ pc ($n_0 = 224 \text{ H cm}^{-3}$ for $\Delta x = 10$ pc) are the local H number density and H number density threshold for star formation respectively. The Schmidt law is used to draw a probability to form a star with a stellar mass of $m_* = \rho_0 \Delta x^3 \simeq 3 \times 10^4 M_\odot$ for the low resolution (*lowRes*) runs and a stellar mass of $m_* \simeq 7 \times 10^3 M_\odot$ for the high resolution (*highRes*) runs (Rasera & Teyssier 2006). The gas temperature in high gas density regions ($n_{\text{gas}} > n_0$) is artificially enhanced by a polytropic equation of state $T = T_0 (n_{\text{gas}}/n_0)^{\kappa-1}$, where $\kappa = 2$ is the polytropic index, and $T_0 = 270 \text{ K}$ for the low and high resolution runs. It is chosen in order to get a constant Jeans length resolved with at least 4 cells. This artificial polytropic equation of state is used to prevent the catastrophic and artificial collapse of the self-gravitating gas (Truelove et al. 1997).

We account for the mass and energy release from type II SNe. The energy injection, which is purely thermal, corresponds to

$$E_{\text{SN}} = \eta_{\text{SN}} \frac{m_*}{M_\odot} 10^{50} \text{ erg}, \quad (2)$$

where $\eta_{\text{SN}} = 0.2$ is the mass fraction of stars going SNe and m_*

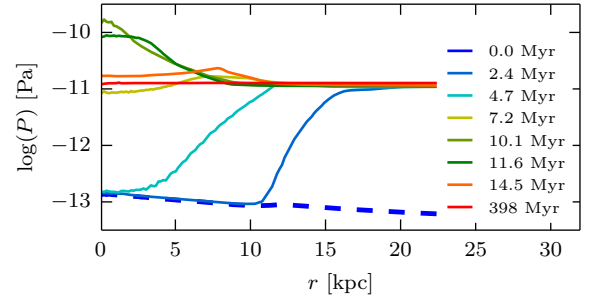


Figure 1. Mean pressure versus radius at different times (see legend) for the pa3 run of the *gasHigh.fb* set. The dashed line shows the pressure profile before the onset of external pressure. The pressures are averaged within spherical shells.

is the mass of the star particle. We also return an amount $\eta_{\text{SN}} m_*$ back into the gas for each SN explosion which occurs 10 Myr after the birth of the star particle. To avoid excessive cooling of the gas due to our inability to capture the different phases of the SN bubble expansion, we use the delayed cooling approach introduced in Teyssier et al. (2013) (in the same spirit as Stinson et al. 2006). The energy of the SN explosion is injected into a passive scalar variable and blocks the cooling of the gas if the corresponding velocity dispersion is larger than $\sigma_{\text{thres}} = 60 \text{ km s}^{-1}$. The energy within that passive scalar decays with a characteristic time-scale of $t_{\text{diss}} = 2 \text{ Myr}$ ($t_{\text{diss}} = 0.5 \text{ Myr}$) for $\Delta x = 40$ pc resolution ($\Delta x = 10$ pc respectively), long enough to block the cooling over a few cell sound crossing times (see Appendix of Dubois et al. 2015).

2.2 Application of external pressure

After adiabatic relaxation (no gas cooling), the origin of time is reset to 0 and the base simulations are run further in time with the subgrid modeling of gas cooling, star formation and feedback, and with an enhanced and uniform pressure outside the disc (*pressure* simulations) for another $\approx 420 \text{ Myr}$. The pressure enhancement is applied at an instant starting at $t = 0$. This instant pressure increase is justified since the bow shock observed in the simulations of Gaibler et al. (2012) manages to pressurise the entire gaseous disc within a time-frame of only a few Myr. The pressure is enhanced in two different configurations: either outside the sphere of radius $r_1 = 12 \text{ kpc}$ (hereafter, *p_spher*), or else where the gas number density is lower than 0.014 H cm^{-3} (i.e. right outside the disc component, hereafter, *p_densor* equivalently *gasHigh.d*). In the *p_spher* simulation, the bow shock pressurising the disc is assumed to be quasi-isotropic. The effect of isotropy of external pressure is compared with a simulation of a non-isotropic bipolar pressure increase in Appendix A.

In the case of spherical geometry (*p_spher*), this pressure enhancement is calculated by

$$P(r, t) = \begin{cases} P(r, 0) & r < r_1, \\ \text{pa} f\left(\frac{r - r_1}{r_2 - r_1}\right) P_{\text{max}} & r_1 \leq r < r_2, \\ \text{pa} P_{\text{max}} & r \geq r_2, \end{cases} \quad (3)$$

where time $t = 0$ is just before the pressure enhancement, pa is the *pressure amplification*, $f(x) = 6x^5 - 15x^4 + 10x^3$ is an increasing function of x starting very gradually at $x = 0$ and smoothly reaching a plateau of unity at $x = 1$, and finally P_{max} is the maximum pressure in the disk at $t = 0$ (reached in the central few cells),

with $P_{\max} \simeq 9.8 \times 10^{-13}$ Pa for the *gasLow* simulation set and $P_{\max} \simeq 4.7 \times 10^{-12}$ Pa for the *gasHigh* and *gasHigh.d* simulation sets. Here, we adopt $r_2 = r_1 + 3$ kpc. This gradual pressure amplification with radius is used to smoothly connect the two pressure regimes. For convenience, we will call paX a simulation run where the pressure amplification is $\text{pa} = X$. This pressure bath is maintained throughout the simulation evolution and is a minimum to the pressure evolved in that region. If the pressure within that bath becomes larger than $\text{pa}P_{\max}$ (due to SNe winds for instance) we take the new value of pressure provided by the Riemann solver. For this *p_spher* case (but also for the *p_dens* case), the simulation of no pressure amplification corresponds to $\text{pa} = P(r_1, 0)/P_{\max} \simeq 0.1$, and we will hereafter denote it as nP (for no pressure enhancement).

For the case of external pressure in disc geometry (*p_dens*), we increase the pressure, only at time $t = 0$, at a value of $\text{pa}P_{\max}$ wherever the gas density is below 0.014 H cm^{-3} . This gas density corresponds to a height of 1.1 kpc above and below the plane along the minor axis of the disk ($R = 0$).

In the simulations of Gaibler et al. (2012), the bow shock that pressurises the disc reaches a maximum pressure of $P \simeq 8 \times 10^{-11}$ Pa. This justifies our chosen pressure enhancement where the maximum pressure increase for the *gasHigh* (pa10) and *gasLow* (pa7) simulation corresponds to $P \simeq 9.8 \times 10^{-12}$ Pa and $P \simeq 3.2 \times 10^{-11}$ Pa, respectively.

The pressure profiles for one of the *p_spher* simulations (run pa3) before and after the pressure enhancement as well as its evolution over the simulation time are shown in Fig. 1. We can see that that at 2.4 Myr, right after the restart of the simulation, the pressure smoothly rises from $\sim 10^{-13}$ Pa at the centre up to 10^{-11} Pa at a distance $r = 13.5$ kpc. At later times, this pressure enhancement propagates within the central region of the halo and connects to the galaxy.

The relevant physical parameters for the pressure simulations are summarised in Table 2.

3 RESULTS

In this section, we present our simulation results considering different isolated disc simulations with various pressure boosts outside the disc. We analyse our simulations regarding disc fragmentation, star formation, clump properties, and the galaxy’s mass budget. We then compare our simulations with a simple theoretical implementation regarding the growth of the star formation rate and show that it scales approximately as the square root of the external pressure. Finally, we calculate the Kennicutt-Schmidt (KS) relation and find that our toy model for AGN-induced over-pressurisation leads to the galaxies lying higher in the starburst region of the KS relation.

The effects of external pressure turn out to be similar whether or not SN feedback is included in the simulations. We will therefore only present, in this section, the results of the stellar feedback simulations. A comparison between the non-feedback and feedback simulations is provided in Appendix B.

3.1 Qualitative differences

Figs. 2 and 3 show maps of the gas density for selected runs at different times, for the *gasLow.fb* and *gasHigh.fb* as well as *gasHigh.d.fb* runs respectively, and for two cases without external pressure boost nP and with extra pressure pa3. Comparing the nP runs, we observe that the gas is clumpier in the *gasHigh.fb* simulation than in the *gasLow.fb* run. We will show in Sect. 3.2 that this

Table 2. Physical parameters of runs: gas fraction (0.1 for *gasLow* and 0.5 for *gasHigh*), pressure amplification (pa), run with no feedback (nf), run with feedback (fb), spatial resolution (Δx), and pressure geometry

Identifier	gas fraction	pa	nf/fb	Δx [pc]	geometry
pa01 \equiv nP		0.1	✓/✓	40	<i>p_spher</i>
pa04		0.4	✓/✓	40	
pa08		0.8	✓/✓	40	
pa1.2		1.2	✓/✓	40	
pa1.5	<i>gasLow</i>	1.5	✓/✓	40	
pa3		3	✓/✓	40	
pa5		5	✓/✓	40	
pa7		7	✓/✓	40	
pa01 \equiv nP		0.1	✓/✓	40	<i>p_spher</i>
pa01_hR \equiv nP_hR		0.1	x/✓	10	
pa02		0.2	✓/✓	40	
pa04		0.4	✓/✓	40	
pa08		0.8	✓/✓	40	
pa1.2	<i>gasHigh</i>	1.2	✓/✓	40	
pa1.5		1.5	✓/✓	40	
pa2		2	✓/✓	40	
pa3		3	✓/✓	40	
pa3_hR		3	x/✓	10	
pa5		5	✓/✓	40	
pa7		7	✓/✓	40	
pa8		7	✓/✓	40	
pa10		10	✓/✓	40	
pa01.d \equiv nP		0.1	✓/✓	40	<i>p_dens</i>
pa02.d		0.2	✓/✓	40	
pa03.d		0.3	✓/✓	40	
pa04.d		0.4	✓/✓	40	
pa08.d		0.8	✓/✓	40	
pa1.2.d	<i>gasHigh</i>	1.2	✓/✓	40	
pa1.5.d		1.5	✓/✓	40	
pa2.d		2	✓/✓	40	
pa3.d		3	✓/✓	40	
pa5.d		5	✓/✓	40	
pa7.d		7	✓/✓	40	
pa10.d		10	✓/✓	40	

is a simple consequence of the Toomre instability. The increased pressure leads to accelerated clump formation for the *gasLow.fb*, *gasHigh.fb*, *gasHigh.d.fb* simulations, and a clumpier ISM in all cases. Generally less gas between clumps in the enhanced pressure runs, in all the *gasLow.fb*, *gasHigh.fb*, and *gasHigh.d.fb* cases can be seen.

In Fig. 3, one can compare the two different ways to increase the pressure (*p_spher*, *p_dens*). The morphological structure of the two simulations *gasHigh.fb* and *gasHigh.d.fb* is slightly different. Fewer clumps are seen in the *gasHigh.fb* run than in the *gasHigh.d.fb* run. It seems, however, that the clumps are only missing in the outskirts of the *gasHigh.fb* galaxy, whereas a similar amount of clumps can be detected in the centre. The edge-on views indicate that in the *gasHigh.fb* simulations, a large amount of mass flows out of the galaxy due to the pressure increase, while in the *gasHigh.d.fb* simulations the mass outflow seems to be less extended. We will quantify the mass outflows in the different runs in Sect. 3.5.

3.2 Disc fragmentation

Since the star formation recipe depends on the local gas density (see eq. 1), we expect enhanced star formation when more clumps

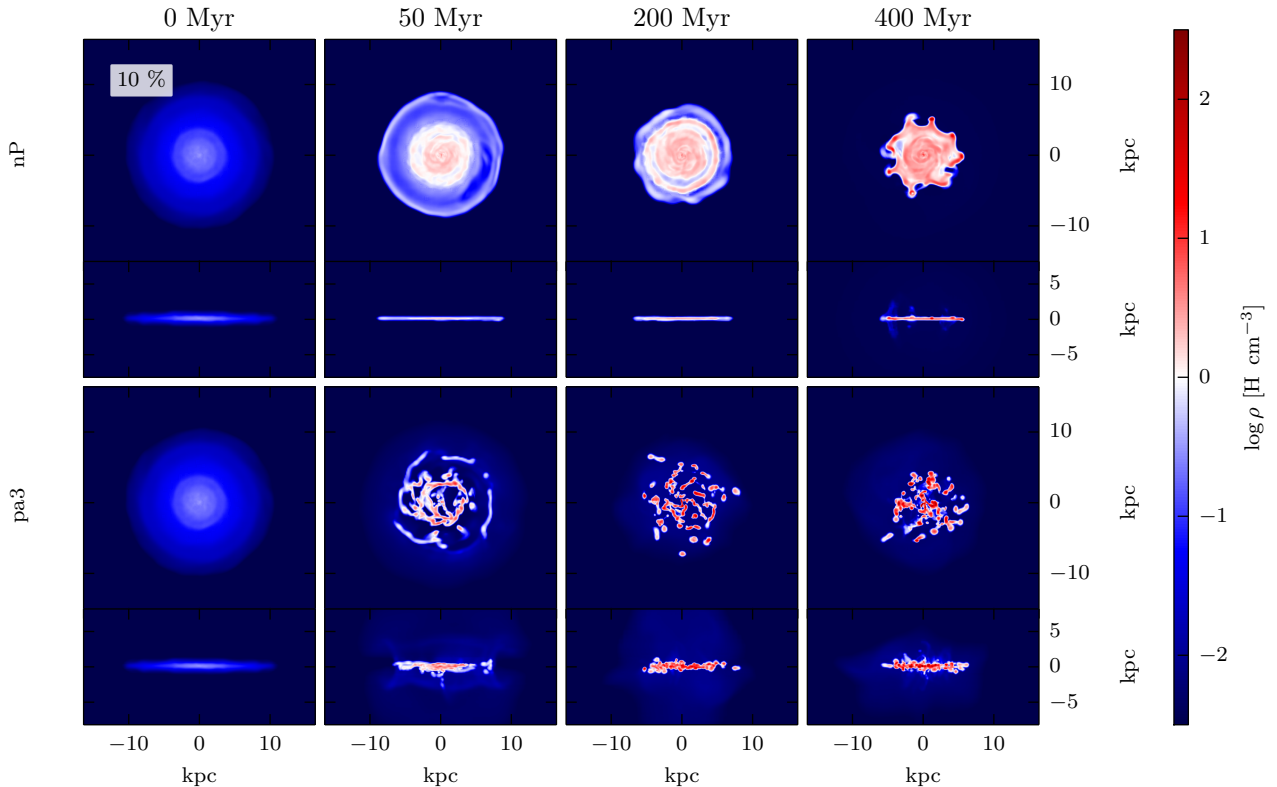


Figure 2. Gas density maps (mass-weighted) of two of the *gasLow_fb* simulations without enhancement of the external pressure nP (top row), and with enhancement of the external pressure pa3 (bottom row). The different columns show different times as labelled. Each panel shows both face-on (40×40 kpc, upper part) and edge-on (40×20 kpc, lower part) views. One can see that an increased pressure outside the galaxy leads to accelerated clump formation and less gas between the clumps.

are formed (as the gas gets more concentrated), assuming that the clumps have sufficient mass. Therefore, if an increased pressure leads to increased fragmentation and hence increased clump formation, we expect star formation to be positively enhanced when external pressure is applied to the galaxy. We first consider the fragmentation by counting the high-density clumps. We detect the clumps in the simulation by running the clump finder described by [Bleuler & Teysier \(2014\)](#). This method identifies all peaks and their highest saddle points above a given threshold (21 H cm^{-3}). A clump is recognised as an individual entity when the peak-to-saddle ratio is greater than 1.5; otherwise the density peak is merged with the neighbor peak with which it shares the highest saddle point.

The visual impression of increased clump formation when external pressure is applied on the galaxy (Figs. 2 and 3), is confirmed when looking at the number of clumps as a function of time. Fig. 4 shows the number of clumps as a function of time for the *gasLow_fb* (left panel), *gasHigh_fb* (middle panel), and *gasHigh_d_fb* (right panel) simulations, respectively.

In the *gasLow_fb* run, the number of clumps is constantly increasing with time, regardless of the amount of external pressure. Clump formation starts earlier in the runs with external pressure. However, the number of clumps at a given time is not a monotonic function of external pressure: at low external pressure (up to pa3), the number of clumps at given time increases with increasing pres-

sure, while the reverse trend occurs for external pressures above $3 P_{\text{max}}$.

The general effect that more clumps are formed in the simulations with external pressure is similar for the *gasHigh_fb* and *gasHigh_d_fb* runs. Similar to the *gasLow_fb* simulation, the number of clumps increases with increasing pressure up to a certain pressure (pa5) and then decreases again for the *gasHigh_fb* simulation and stays at the same level for the *gasHigh_d_fb* simulation. For the lower pressure as well as the non-pressure simulations, the number of clumps increases with time. However, for higher pressure simulations, the number of clumps reaches a plateau at late times. For the *gasHigh_fb* runs, the initial rise in the number of clumps is fastest for the pa3, pa5 and pa7 cases, but in the pa3 case the number of clumps reaches its plateau at a later time, hence at a higher level.

The time evolution of the number of clumps for the *gasHigh_d_fb* simulation is roughly similar to the *gasHigh_fb* simulation. At early times, the rise in number of clumps is fastest for the high pressure runs. The number of clumps keep rising with time for the lower pressure enhancements, while it reaches a maximum for the higher pressure enhancements. The time when the number of clumps reaches its plateau is also shortest for higher external pressures. After 300 Myr, there is no clear trend in number of clumps versus external pressure for the higher pressure runs. The increase of clump number is therefore highly dependent on the

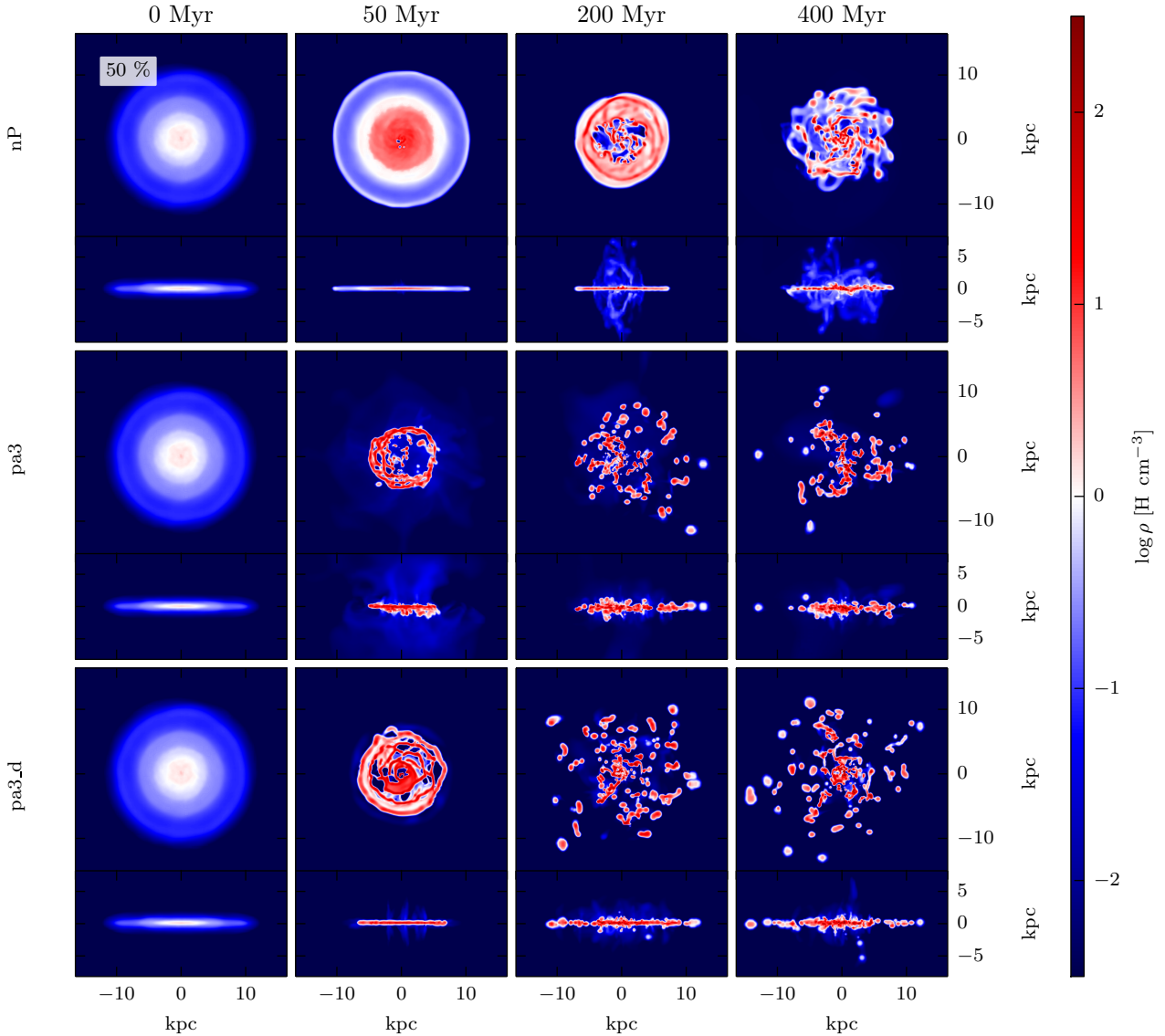


Figure 3. Gas density map (mass-weighted) for a selection of the *gasHigh.fb* and *gasHigh.d.fb* simulations, for no pressure enhancement (top), and for a pressure enhancement of pa3 (middle for *gasHigh.fb* and bottom for *gasHigh.d.fb*). The density scale is as in Figs. 2. An increased pressure outside the galaxy leads to accelerated clump formation and less gas between the clumps. The morphological structure of the two simulations with two different ways to increase the pressure (*gasHigh.fb*, and *gasHigh.d.fb*) is slightly different, but only in the outskirts of the galaxy. The edge-on view shows a mass outflow for all the simulations.

pressure applied on the galaxy. However, beyond a certain pressure enhancement (pa5_d), the number of clumps remains very similar for higher pressure runs. After ≈ 300 Myr the number of clumps is roughly independent of external pressure for the *gasHigh.fb* and *gasHigh.d.fb* simulations.

In the *gasLow.fb* run with no external pressure, only a single clump in the entire disc is formed, at late times (350 Myr), when the gas has sufficiently collapsed to reach the clump gas density threshold. On the contrary, in the *gasHigh.fb* run, the number of clumps increases up to $\simeq 35$, even without any forcing by the external pressure.

The difference between the gas-poor and gas-rich galax-

ies, before the external pressure is applied, is that the gaseous disc is Toomre-stable against small-scale fragmentation in the gas-poor case where the mean Toomre parameter is $\langle Q \rangle = \langle c_s \kappa / (\pi G \Sigma_{\text{gas}}) \rangle = 3.29 > 1$, while the gas-rich disc is Toomre-unstable with $\langle Q \rangle = 0.72 < 1$ (see Fig. 5). Here, Σ_{gas} is the surface density, c_s is the sound speed, and κ is the epicyclic frequency (measuring the shear of the rotating disc). Therefore the *gasLow.fb* simulations demonstrate that fragmentation of the galactic disc can be driven by the forcing of an external pressure, even though the disc is initially Toomre-stable.

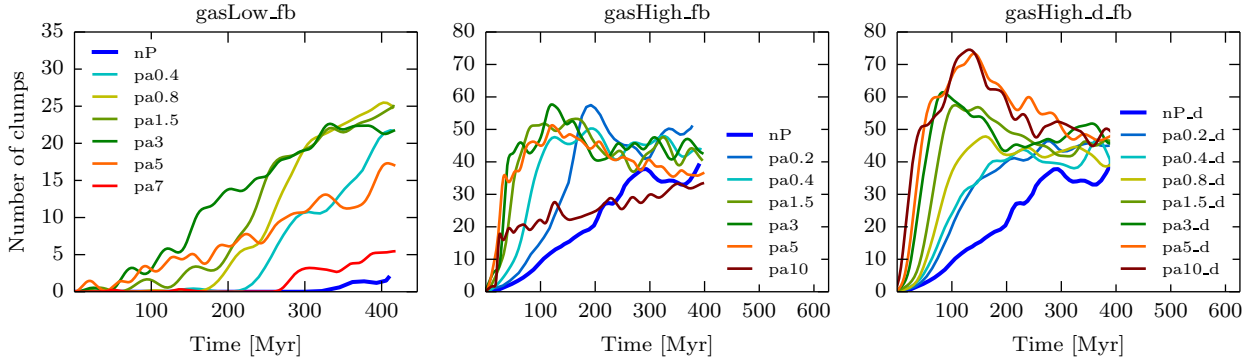


Figure 4. Time evolution of the number of clumps for a selection of simulations with supernova feedback: *gasLow_fb* (left), *gasHigh_fb* (middle), and *gasHigh_d.fb* (right) simulations. The lines are smoothed with a Blackman-Harris window with a width of $2\sqrt{\text{len}(\text{array})}$, where $\text{len}(\text{array})$ is the number of points. The clumps were extracted with the Bleuler & Teyssier (2014) algorithm, with a density threshold of $21 H \text{ cm}^{-3}$ and a peak-to-saddle threshold of 1.5. The maps show that an increased pressure leads to increased clump formation and the increase in clump number is dependent on the pressure applied onto the galaxy. Beyond a certain pressure enhancement, the number of clumps decreases or remains very similar for higher pressure runs.

3.3 Star formation history

In Sect. 3.2, we have seen that an increased pressure enhancement leads to an increased number of clumps up to a certain time and then a typically lower number of clumps thereafter. Since the gas density threshold of clump detection is set to be above that for star formation, one expects that the star formation history should evolve in a similar fashion to the evolution of the number of clumps.

Fig. 6 shows that the star formation histories of the different runs indeed resemble the time evolution of the number of clumps previously shown in Fig. 4. In particular, at early times in the runs with *gasHigh* higher pressures lead to higher SFRs. But with high pressures, the SFR saturates earlier. In the *gasHigh_fb* runs, the

maximum SFRs in the high pressure runs are lower than in the other runs, while in the *gasHigh_d.fb* runs, the maximum level of SFR is reached for the three highest pressures, while the SFRs at later times (300 Myr) are roughly independent of the external pressure.

In the *gasLow_fb* runs, while the nP case leads to star formation only after a long time delay (330 Myr), the highest pressures, although leading to immediate but small levels of star formation, are unable to generate substantial star formation from the earliest times. The runs with intermediate pressures produce the highest SFR at all times. We will show in the next sections that this is due to the low mass-outflow of the intermediate pressure simulations that allows the clumps to increase in density. Conversely, larger

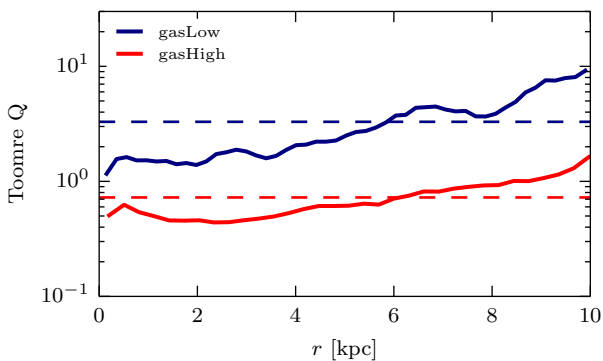


Figure 5. Local Toomre parameter for the relaxed disc at $t = 0$ for the *gasLow* and *gasHigh* simulations. The dashed line shows the mean Toomre parameter of the disc for the *gasLow* simulation $\langle Q \rangle = 3.29 > 1$ and for the *gasHigh* simulation $\langle Q \rangle = 0.72 < 1$. One therefore expects the *gasHigh* simulation to fragment independently of external pressure enhancement whereas the *gasLow* simulations are not expected to fragment into many clumps. The fact that the pressur-enhanced simulations of the *gasLow* galaxies shows a significant increase in the number of clumps compared to no-pressure enhancement demonstrates that external pressure can stimulate the fragmentation of a disc even if it is Toomre-stable.

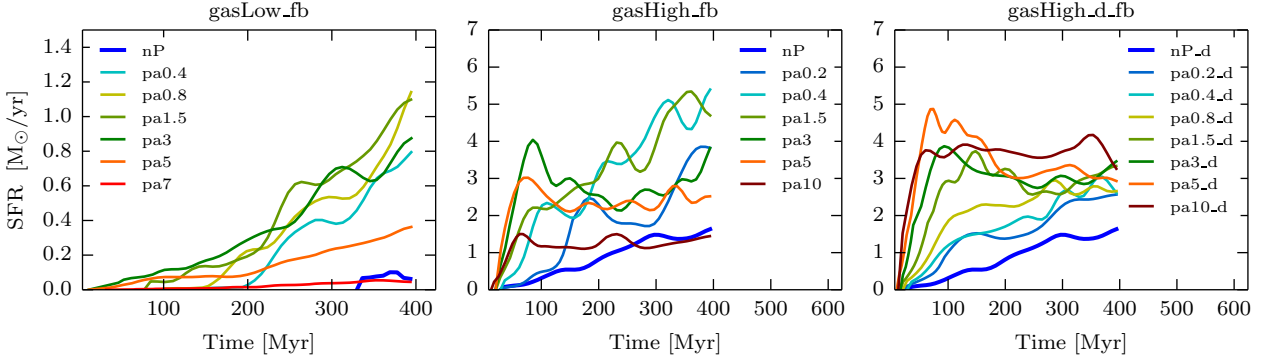


Figure 6. SFR for a selection of the simulations with supernova feedback: *gasLow_fb* (left), *gasHigh_fb* (middle), and *gasHigh_d_fb* (right) simulations. The lines are smoothed as in Figure 4. This figure shows that higher pressures lead to higher SFRs. For the higher pressure enhancement simulations, the SFR reaches a maximum or plateau at later times for the *gasHigh_fb*, and *gasHigh_d_fb* simulations. After a certain pressure increase, the SFR decreases or stays at the same level for all the simulations and hence the runs with intermediate pressure generally produce the highest SFR at all times.

external pressures lead to such strong pressure waves that the gas is removed from the galaxy. This prevents the formation of large clumps and tends to suppress the star formation.

The effect of the external pressure on the SFR is even more significant when looking at the *gasHigh_fb* simulations (middle panel of Fig. 6). The SFR of the no-pressure simulation slowly increases after a certain time, whereas the SFR increases faster when pressure is applied: it reaches a maximum at a certain rate and more or less maintains this rate for the remaining of the simulation. Towards the end of the simulation, the SFR of the no-pressure simulation catches up, again similarly to the clump number behaviour. The SFR for the *gasHigh_d_fb* simulation (right panel of Fig. 6) behaves quantitatively similar to the *gasHigh_fb* simulation. One can see that the SFR in these simulations reaches the maximum or plateau at later times than in the corresponding *gasHigh_fb* simulations. The rapid rise of the SFR reaches increasingly higher levels of peak SFR with higher external pressure up to *pa5_d*, while *pa10_d* reaches a slightly lower maximum SFR.

The left panels of Fig. 6 show that the SFRs of the *gasLow* simulations start with a significant time delay, and the maximum enhancement of the SFR relative to the nP run is highest (~ 12) at the end of the simulation (after 400 Myr). On the other hand, the corresponding SFR enhancements for the higher gas fraction simulations (middle and right panels of Fig. 6) are lower (~ 3.5 for *gasHigh* and ~ 1.5 for *gasHigh_d*) at the end of the simulation (after 400 Myr) than at the beginning (~ 40 for *gasHigh* and ~ 70 for *gasHigh_d* at ~ 80 Myr) of the simulation. External pressure thus first produces a significantly higher SFR in comparison to the simulation with no external pressure. But the duration of this large SFR enhancement for the *gasHigh* and *gasHigh_d* simulations is shorter than that of the *gasLow* simulation. The free fall time of the higher density gas is shorter than the free fall time of the low density gas which leads to the gas collapsing early on, whereas a delay is expected for the lower gas fraction disc.

3.4 Clump Properties

An important SFR requires a significant supply of cold gas as well as the fragmentation of the disc into clumps that carry a sufficient amount of gas to form stars. On the other hand, one can argue with

the Jeans and Toomre instability arguments if indeed an increased pressure outside the galaxy that later increases the pressure inside the galaxy leads to higher densities, as well as a possible expulsion of disc gas depending on the momentum carried by the pressure wave coming into the disc. The competition between higher densities and mass outflow will influence the amount of gas within the clumps.

For the gas-rich disc simulations, we saw (Fig. 4) that, at the very beginning, when the pressure wave comes into the galaxy, the number of clumps is highest for the highest pressure. While the clumps are more numerous with the highest pressures, it is worthwhile knowing whether their masses are affected by the external pressure.

Fig. 7 shows the modulation of the average clump mass rises with external pressure at three times of the simulations. At early times (top panel), the clump masses for the *gasHigh* simulations (*gasHigh*, center panel, and *gasHigh_d*, right panel) are higher the greater the external pressure. At later times (middle and bottom panel), the clump masses are roughly independent of the external pressure applied, probably because the disc gas has been either already accreted onto the clumps or expelled out of the galaxy (see discussion below), leaving no more diffuse gas available for accretion onto the clumps. The time at which the diffuse gas is either consumed onto the clumps or expelled must happen earlier for the higher external pressure simulations as the fragmentation happened earlier for these simulations. This explains the different times when the SFR reaches a plateau, occurring earlier the higher the pressure. In the *gasHigh_fb* runs at high external pressures, fragmentation is not the only cause of SFR (since there is a maximum pressure enhancement beyond which the SFR is lower), meaning that the gas supply is more critical, and not always available despite the high gas fraction. This suggests that the mass flow out of the galaxy also plays an important role. And indeed, the mass outflow is very efficient for *pa7* and *pa10* after 30 Myr. We will discuss this in detail in Sect. 3.5, below.

In the *p_dens* simulations, there is a maximum pressure enhancement (*pa5_d*) beyond which the SFR remains at approximately the same level without decreasing. As we will see in Sect. 3.5, mass outflows are also absent. The high gas fraction leads therefore to higher density enhancement by external pressure,

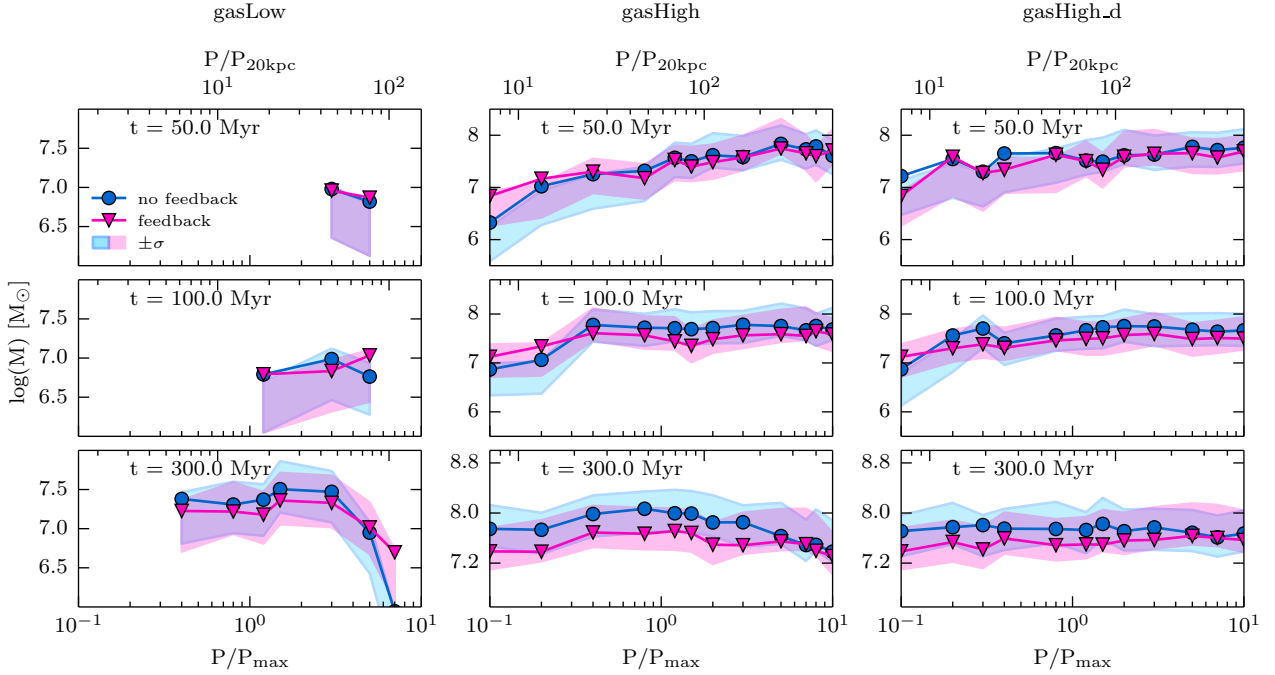


Figure 7. Average clump mass for the *gasLow.fb* (left), *gasHigh.fb* (middle), and *gasHigh_d.fb* (right) simulations. The orange line with round markers correspond to the non-feedback simulations whereas the pink line with triangles corresponds to the feedback simulations. The shaded green/blue area shows the area of mass containing $\pm\sigma$ of the density PDF for the no-feedback/feedback simulations. In the bottom and top of each subfigure, the x-axis shows the P/P_{\max} and $P/P_{20\text{ kpc}}$ values respectively, where P_{\max} is the maximum pressure inside the disk and $P_{20\text{ kpc}}$ is the averaged pressure at 20 kpc. At the beginning of the simulation, the clump masses for the *gasHigh* simulations are higher the greater the pressure for the *gasHigh* simulations. At later times, the clump masses are roughly independent of the external pressure. For the *gasLow* simulation, the clump mass does not increase with higher external pressure but rather decreases or stays at approximately the same level.

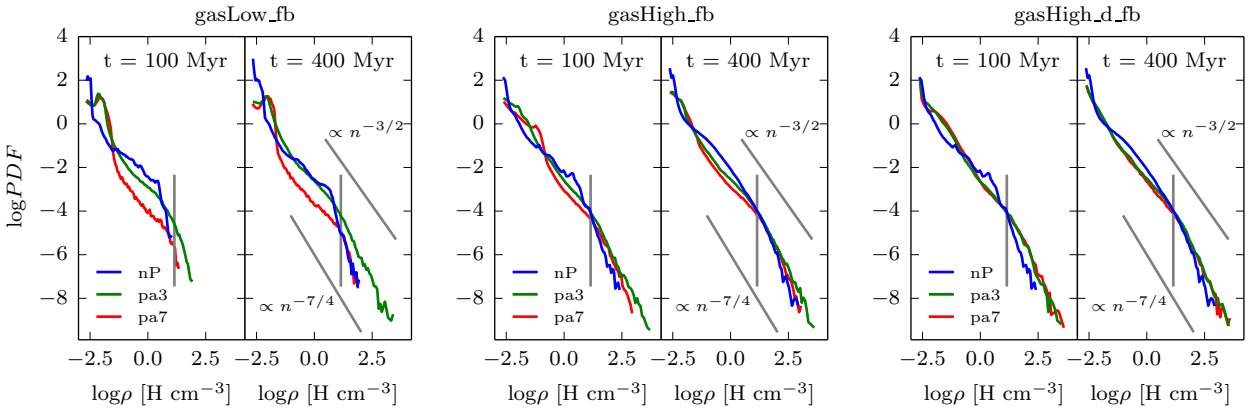


Figure 8. Density PDF at different times for a selection of the *gasLow.fb* (left), *gasHigh.fb* (middle) and *gasHigh_d.fb* (right) simulations. The threshold (14 H cm^{-3}) for star formation is plotted as a grey vertical line. One can see that greater external pressure allows the galaxy to reach higher densities on a faster time-scale. The nP simulation slowly catches up with the over-pressure simulations for the *gasHigh* whereas this is not the case for the *gasLow* simulation. For the *gasLow* simulation, the high pressure simulation (pa7) never reaches the high densities. As indicated with the grey power law lines one can see that over the course of the simulation a slope between $-3/2$ and $-7/5$ (or even steeper) develops at high densities. This is in agreement with simulations including gravity and turbulence done for instance by Kritsuk et al. (2011).

hence both number of clumps and SFR are highest when the external pressure are high. However, there only is a limited amount of gas available in the galaxy. One can assume that the limited gas supply is insufficient for more star formation, so the SFR remains at the same level independently of the pressure enhancement.

Fig. 7 shows that, for the *gasLow* simulations (*gasLow*, left panel), the clump mass does not increase with greater external pressure, but rather decreases at early times (top panel). At later times, the clump mass is roughly independent of the pressure up to $\text{pa}3$, beyond which the clump mass decreases. This is the same pressure enhancement which leads to the highest SFR. As we will see in Sect. 3.5, the *gasLow* galaxies suffer from strong gas outflows that reduce the supply of gas available for clump buildup, leading in turn to smaller clump masses within the galaxy.

In Fig. 7, the difference in clump masses for the feedback and non-feedback simulations can also be seen for all the simulations. At early times, there is a significant difference between the no-feedback and feedback simulations. At later times, the difference in clump masses becomes more apparent for both the high gas fraction and *gasLow* simulations. One can see that the clump masses for the feedback simulations are lower at the end of the simulation than for the no-feedback simulations, independent of the pressure increase. Because the feedback increases the porosity of the interstellar medium that in turn counteracts the formation of clumps (Silk 2001), the observed smaller clump masses for the feedback simulations are expected. This difference is more dominant in the *gasHigh* simulation as can be seen in the left panel of Fig. 7. The similar mean clump masses in the feedback and non-feedback runs at the beginning of the simulation appears to be a consequence of the implementation of the SNe in the simulation. As discussed above, a SN explosion occurs 10 Myr after the birth of the star particle. The first stars form shortly before 50 Myr and one would therefore not expect to see a large difference between the feedback and no-feedback simulations. At 100 Myr, some stars exploded into SNe, but only constitute a small fraction of all stars, hence the small difference between the feedback and no-feedback simulations at this stage.

It is interesting to look at the density probability function (PDF) at different times of the simulations in order to better understand the observed SFR behaviour. The PDF can be seen in Fig. 8 for two different times for a selection of the *gasLow* (left), *gasHigh* (middle), and *gasHigh.d* (right) simulations. Increasing external pressure allows one to reach higher gas densities faster, which is in agreement with the SFR behaviour we have seen previously. For the *gasHigh* simulations, the nP simulation slowly catches up with the over-pressure simulations similar to the SFR behaviour. For the *gasLow* simulation, the no-pressure simulations never attain the densities reached by the moderate pressure enhancement simulations. The high pressure simulation ($\text{pa}7$) also never reaches high gas discuss in Sect. 3.5, below. It can be seen in Fig. 8 that over the course of the simulation a high density power law with a slope between $-7/4$ (or even steeper) and $-3/2$ develops, especially for the high gas fraction simulations. A comparable power law range has been found in observations (e.g., Kainulainen et al. 2009, Lombardi et al. 2010) and simulations including gravity and turbulence (e.g., Kritsuk et al. 2011) where they argue that the origin of the power law tail is due to self-similar collapse solutions.

3.5 The Galaxy's Mass budget

The mass flow rate (MFR) as well as the total amount of newly formed stars plus dense gas should provide us a better understand-

ing of the star formation history described above. In particular, one would like to understand why there seems to be an optimal external pressure enhancement for star formation, beyond which the SFR ends up at lower values.

We measure the gas mass flux through a sphere of radius 16 kpc as

$$\dot{M}_{\text{gas}} = \iint \rho \mathbf{v} \cdot \hat{\mathbf{r}} \, dS = \sum_{i \in \text{shell}} m_i \mathbf{v}_i \cdot \hat{\mathbf{r}}_i \frac{S}{V}, \quad (4)$$

where i denotes the index of a cell within a spherical shell of surface S and volume V . Here, we adopt a shell of thickness 4 kpc. The MFR is shown in Fig. 9 for the *gasLow.fb* (left), *gasHigh.fb* (middle), and *gasHigh.d.fb* (right) simulations, again only for the simulations with SN feedback. The top panels show the mass flow, while the bottom ones show the cumulative mass flow in fractions of the total gas mass within the 16 kpc sphere before the pressure increase shown on the bottom. We will discuss the effects of SN feedback in Appendix B.

In all three sets of simulations, external pressure leads to mass inflow at early times. This early mass inflow is large but different for the different ways pressure is applied onto the galaxy. In the *p_spher* simulations, the pressure is applied outside the galaxy in a low density medium leading the pressure to have a larger pressure gradient than in the *p_dens* simulations where the pressure is applied close to the galaxy and therefore in a higher density environment. This larger pressure gradient in the *p_spher* simulations, allows the pressure wave to carry more mass and momentum from the ambient hot medium in comparison to the pressure wave of the *p_dens* simulations. This explains the larger mass inflow observed in the *p_spher* simulations (left and middle panels of Fig. 9) compared to that at the start of the *p_dens* simulation. With its larger momentum, the mass inflow of the *p_spher* pressure wave is followed by a short period of mass outflow (for both low and high gas fractions). This mass outflow is negligible for the *gasHigh.d.fb* simulations, since the pressure wave carries very little momentum.

For the *p_spher* simulation sets, higher external pressures lead to stronger maximum inflows at early times and to stronger maximum outflows at later times. In addition, in the simulations with high external pressures ($\text{pa}7$ and $\text{pa}10$), the mass outflow that follows the mass inflow occurs very rapidly (in less than 20 Myr). After these two phases of important mass inflow/outflow, the MFR oscillates around zero for both the *gasLow.fb* and *gasHigh.fb* simulations with $\text{pa} < 5$. In contrast, in the *gasHigh.d.fb* simulations, the MFR depends little on the external pressure.

It is also instructive to consider the evolution of the cumulative gas mass flow through the 16 kpc sphere (bottom panels of Fig. 9) shown relative to the initial mass within the sphere of that radius. The cumulative mass flow remains negative (e.g. mass inflow) for all *gasLow.fb* simulations. The cumulative mass flow for the *gasHigh.fb* with low external pressures ($\text{pa}0.2$ and $\text{pa}0.8$) remain negative, while for higher external pressures, they end up positive. Whereas for low external pressure ($\leq \text{pa}3$) the cumulative mass outflow is less than 5% of the initial gas mass, the cumulative mass outflow reaches 80% of the initial gas mass for the highest external pressure simulation $\text{pa}10$. Finally, all simulations in the *p_dens* geometry lead to cumulative mass inflow at all times, with the strongest cumulative inflows occurring for the runs with the greatest external pressures. We stress, however, that the pressure and no-pressure *p_dens* simulations do not differ significantly and that, overall, there is little net mass flow. This most likely explains why the SFR of the *p_dens* simulations is smoother and less

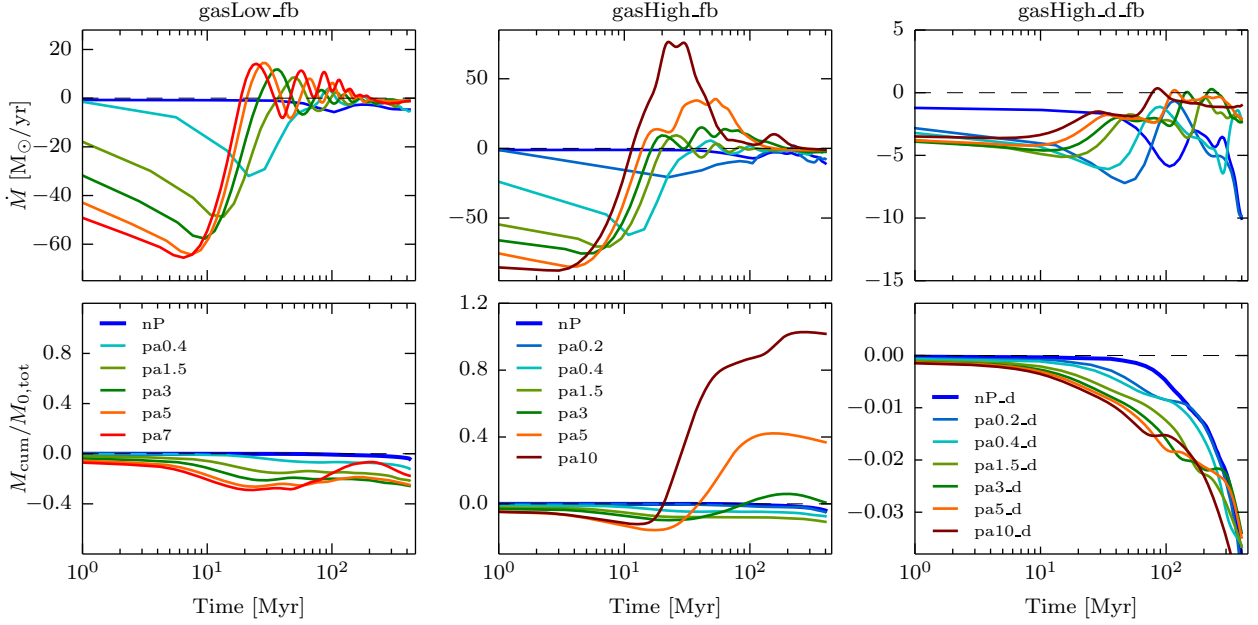


Figure 9. Time evolution of the mass flow rate (top) and cumulative mass flow relative to the initial mass $M_{0,\text{tot}}$ before inputting the pressure (bottom), both at 16 kpc from the galaxy center (where the initial mass is within a sphere of that radius), for selected runs from the *gasLow_fb* (left), *gasHigh_fb* (middle) and *gasHigh_d_fb* (right) simulations. Negative (positive) values of the mass outflow rate denote a net mass inflow (outflow). One can see a difference in the mass flow rate (MFR) between the different ways pressure is put on the galaxy (*gasHigh_fb*, *gasHigh_d_fb*). Due to the pressure gradient in the *p_spher* simulations, the pressure wave coming into the galaxy carries a lot of momentum that leads to a mass inflow followed by a mass outflow for the higher pressure simulations. This mass outflow is negligible for the *p_dens* simulations due to the pressure wave carrying very little momentum. For the most extreme case, the expelled mass reaches 80% of the initial gas mass for the highest external pressure simulation of *gasHigh_fb*.

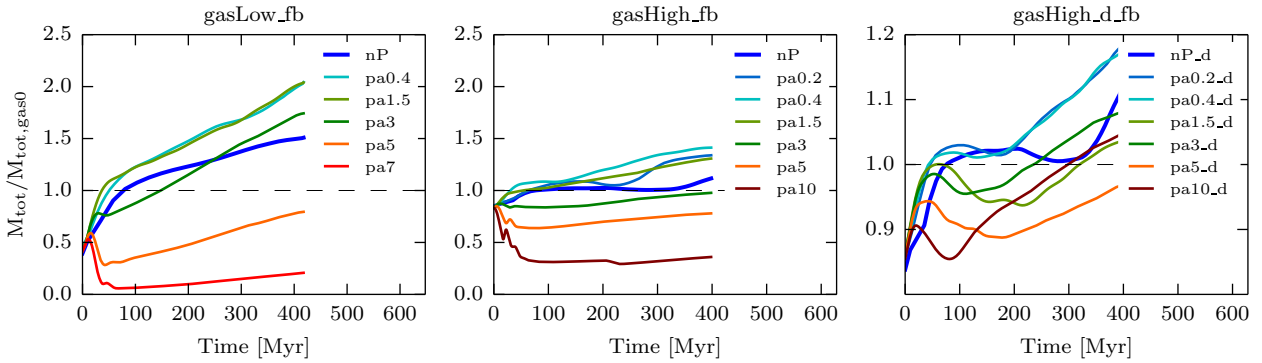


Figure 10. Time evolution of the mass in newly formed stars plus dense ($n > 0.1 \text{ H cm}^{-3}$) relative to the initial gas mass for a selection of the simulations with SN feedback: *gasLow_fb* (left), *gasHigh_fb* (middle), and *gasHigh_d_fb* (right) simulations. The lines are smoothed as in Figure 4. Due to the mass inflow shown in Fig. 9, at the beginning of the simulation more mass can end up in the galaxy. This extra mass of gas is more significant for the *gasLow* galaxy for both the no-pressure and low-pressure enhancement simulations. For high pressure enhancement in the *gasLow* simulation, the incoming pressure wave significantly disperses the galactic gas. The evolution of M_{tot} is similar for the *gasHigh_fb* simulation albeit with less mass variation. For the *gasHigh_d_fb* simulations, no significant mass variation within the galaxy due to pressurisation is observed.

noisy when compared to the *p_spher* simulations of the same gas fraction (*gasHigh*).

In order to understand the galaxy's mass budget better we look at the time evolution of the total mass of newly formed stars plus dense ($n > 0.1 \text{ H cm}^{-3}$) gas, $M_{\text{tot}} = M_{\text{tot},\text{starsN}} + M_{\text{tot},\text{gasD}}$ is

shown relative to the initial galaxy gas mass (total not just dense), $M_{\text{tot},\text{gas0}}$ (see Table 1) shown in Fig. 10. The initial value of $M_{\text{tot}}/M_{\text{tot},\text{gas0}}$ is below unity at $t = 0$ since the gas density in the galaxy is not everywhere above $n > 0.1 \text{ H cm}^{-3}$, especially in the outskirts of the disc and for the *gasLow* galaxy. In the ab-

sence of extra external pressure (nP runs), the ratio $M_{\text{tot}}/M_{\text{tot,gas0}}$ quickly moves significantly beyond unity as the gas cooling allows to reach the gas densities above $n > 0.1 \text{ H cm}^{-3}$. The gas cooling also takes place in the circumgalactic medium that feeds the galaxy with some extra gas. This extra mass of gas adds more significantly to the low-gas fraction galaxy because of its lower initial gas mass, which explains why the increase is more significant in the *gasLow* runs than in the *gasHigh* runs.

For the *gasLow* simulations, intermediate regimes of forced external pressure (from pa0.4 to pa3) also show values of $M_{\text{tot}}/M_{\text{tot,gas0}}$ above 1 with values comparable to the nP run. Therefore, the increase in SFR (an order of magnitude above nP) is to be attributed to the extra compression of the ISM and exploration of larger gas densities with shorter collapsing time-scales (see Fig. 8). In contrast, higher pressurisation values of the ISM (pa5 and pa7) lead to strong gas removal due to the incoming pressure wave that manages to significantly disperse the galactic gas. Since the gas reservoir is reduced, the SFR is also suppressed compared to more intermediate regimes of pressurisation, but the overall SFR is still larger than in the nP case, where gas fragmentation is not reached.

The evolution of $M_{\text{tot}}/M_{\text{tot,gas0}}$ in the *p-spher gasHigh* galaxy behaves similarly to that for the *gasLow* galaxy, although with lower mass variation. It starts below unity for all pressures, and decreases even more for the high pressure increases (pa5 and pa10), because of the large mass outflows observed for those runs. This shows that the large mass outflows associated with high pressures prevent star formation. On the other hand, $M_{\text{tot}}/M_{\text{tot,gas0}}$ keeps rising for the lower pressure enhancements, showing that because no large mass outflow is observed, more stars can be formed. The $M_{\text{tot}}/M_{\text{tot,gas0}}$ curve is higher when a small pressure is applied outside the galaxy compared with the no-pressure simulation. In the case of *p-dens* over-pressurisation, there is no significant (< 20 percent relative) mass variation in the galaxy. Thus, the early fragmentation due to the increased pressure drives the different SFR levels for the different pressure simulations.

3.6 The Star Formation Rate

We expect the SFR to scale as the square root of the external pressure, at least in the *gasHigh* case, for the following reason. The Kennicutt (1998) star formation relation is generically fit by

$$\dot{\Sigma}_* = \frac{\epsilon \Sigma_g}{t_{\text{dyn}}}, \quad (5)$$

for theoretical and observational reasons (Elmegreen 1997; Silk 1997; Genzel et al. 2010). In equation (5), Σ_* is the surface density of star formation, Σ_g is the gas surface density, ϵ is a dimensionless normalisation constant, and t_{dyn} is the dynamical time (the rotation time for a disk galaxy or the free-fall time for a giant molecular cloud, both classes of objects fitting the correlation Krumholz et al. 2012). The slope of the correlation corresponds to the linear theory-inspired convolution of gas density and the most rapidly growing gravitational instability rate for a cold disk. Much more physics resides in the normalisation, ϵ , which is a measure of the star formation efficiency, often defined as the fraction of gas turned into stars per dynamical time, and in the dispersion. We will not address the dispersion here, other than to remark that physics beyond a density threshold must be included, as is evident from the low (e.g. central molecular zone Kruijssen et al. 2014) and high (both in nearby, cf. Leroy et al. 2015; Turner et al. 2015 and distant, cf. Finkelstein

et al. 2015; Dye et al. 2015) outliers. The usual fit to the normalisation is $\epsilon \approx 0.02$, to star-forming systems out to $z \sim 2$, although there is recent evidence that the efficiency is significantly higher in starburst galaxies at higher redshift. The logical generalisation to go beyond a density threshold is to include turbulence (Padoan & Nordlund 2011; Hennebelle & Chabrier 2011; Hopkins et al. 2013). An especially simple implementation is given in Silk (2001); Silk & Norman (2009). We will now extend their argumentation of momentum injection by SNe to an injection of energy by any kind of process that affects the whole galaxy (e.g. energy injection given by external pressure).

Let E_{inj} be the kinetic energy injection given for instance by a pressure wave coming into the galaxy. In the same fashion let $m_{\text{inj}}v_{\text{inj}}$ be the momentum injection. We now make the educated assumption that the energy injection affects the interstellar clouds. These clouds acquire terminal velocity given by

$$\sigma_g = \epsilon v_{\text{inj}} \frac{t_{\text{coll}}}{t_{\text{dyn}}}, \quad (6)$$

where t_{coll} is the cloud collision timescale and v_{inj} is the specific momentum injected. We immediately see that the key efficiency parameter ϵ is proportional to the gas turbulence velocity σ_g . There are recent indications that star formation efficiency increases in highly turbulent environments (Leroy et al. 2015). With momentum balance and Eq. (6), we get

$$\frac{\dot{\Sigma}_* E_{\text{inj}}}{m_{\text{inj}} v_c} = \frac{f_c \Sigma_g \sigma_g}{t_{\text{coll}}}, \quad (7)$$

where σ_g is the gas velocity dispersion, v_c the cloud velocity and f_c the cloud volume filling factor. We however ignore complications with f_c and define it directly by the cold gas fraction f_g . Also, we assumed $v_{\text{inj}} \propto v_c$, with v_c being the velocity of the cloud. We can rewrite the star formation rate per unit volume as

$$\dot{\rho}_* = \epsilon_{\text{inj}} f_g \sqrt{G \rho_g} \rho_g \quad (8)$$

with $\epsilon_{\text{inj}} = (m_{\text{inj}}v_c\sigma_g)/E_{\text{inj}}$.

For the present purpose, we note that the SFR can be rewritten as

$$\dot{\rho}_* = \frac{\epsilon_{\text{inj}}}{\sigma_g} G^{1/2} \rho_g p_{\text{turb}}^{1/2}, \quad (9)$$

where we used $p_g = \rho_g \sigma_g^2$ and assumed that $p_g \propto p_{\text{turb}}$, with p_{turb} being the turbulent pressure induced by the injection.

Hence, we expect that AGN-induced pressure should provide a boost of the star formation rate, independently of any possible increase in star formation efficiency, and initially vary as the square root of the pressure boost. This effect should be important for the gas-rich simulations as gas turbulence plays a lesser role in contributing to a gas-poor disk and the assumption that the gas pressure scales with the gas turbulence breaks down. This is because we omitted the cold cloud mass fraction in the simple formulation above, and the molecular hydrogen fraction decreases at lower gas pressure (Blitz & Rosolowsky 2006).

Fig. 11 illustrates how the SFR increases in time as a function of the external pressure. The mean SFR is calculated from a linear fit of the SFR from time $t = 0$ to time t . For the *gasLow*, *gasHigh*, and *gasHigh.d* simulation sets, the SFR increases with increasing external pressure until a maximum is reached and then decreases again or stays at a similar level as for the *gasHigh.d* simulations. Also, no significant difference in the SFR can be seen between the feedback and non-feedback simulations, indicating that the external pressure increase is the dominant effect driving the increased SFR.

In order to compare with the prediction explained above, a

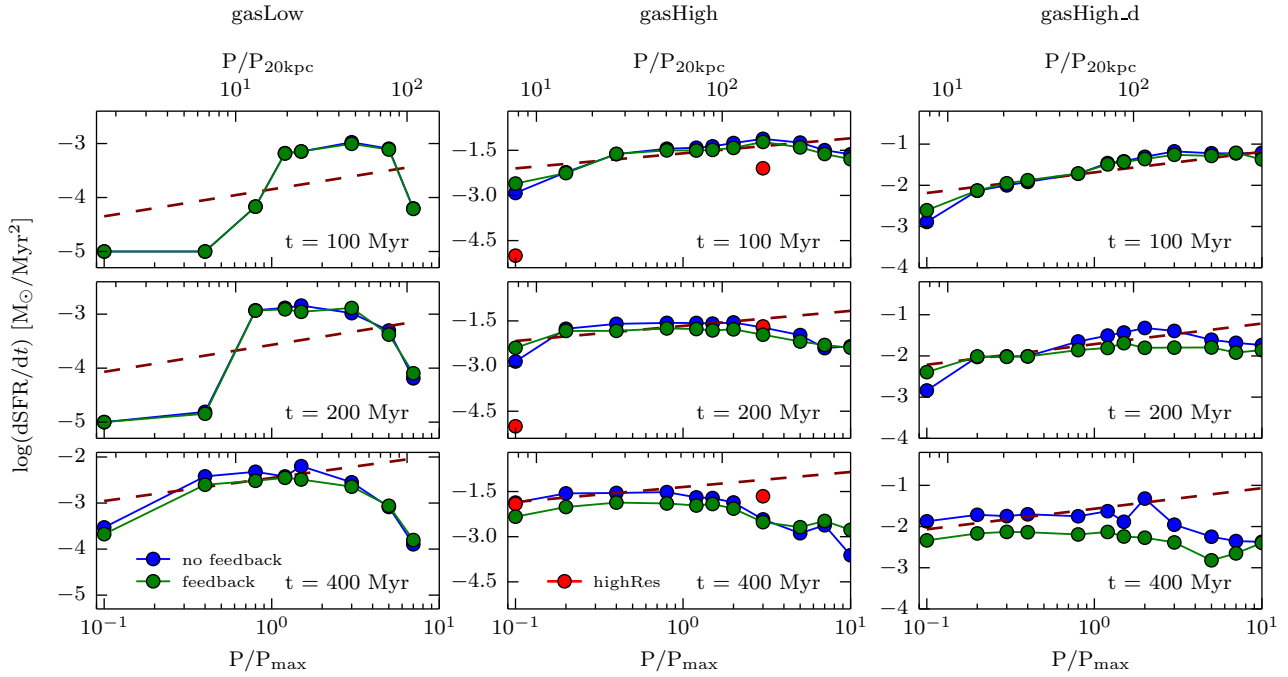


Figure 11. Time evolution of the average rate of increase of the star formation rate for all the *gasLow_fb* (left), *gasHigh_fb* (middle), and *gasHigh_d_fb* (right) simulations. Here, the no-feedback simulations are shown in blue and the feedback simulations are shown in green. The average rate of increase is calculated from a linear fit of the SFR from $t=0$ to three different times. The red points are the corresponding points from the *highRes* runs. The linear fit has been performed on the smoothed SFR data. The SFR data are smoothed as in Figure 4. The dark red-dashed straight lines correspond to visual fits with a slope 1/2 to guide the eye. One can see that for higher gas fraction simulations, the SFR growth rate increases with external pressure and follows the square root of external pressure. At later times, this is only true up until a certain external pressure. For the low gas fraction simulation, the SFR growth rate does not scale with the square root of the external pressure.

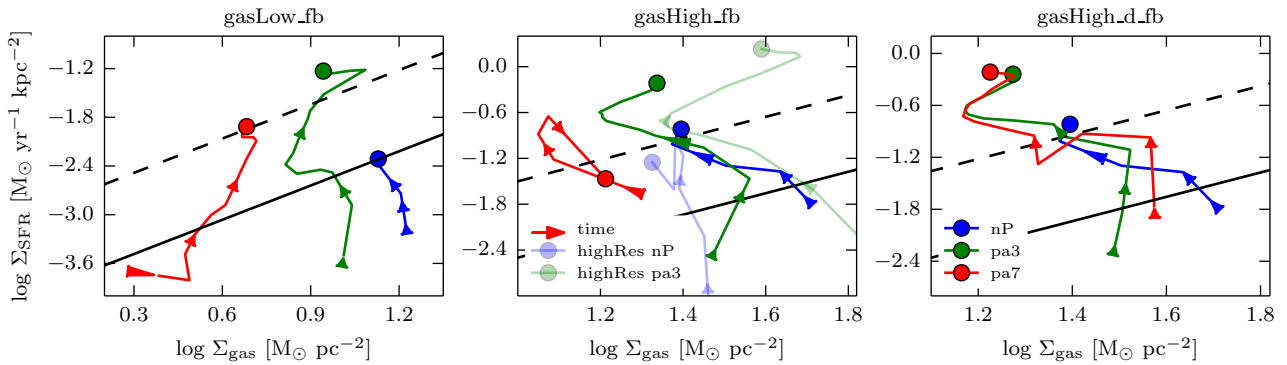


Figure 12. Kennicutt-Schmidt (KS) relation for selected runs (nP, pa3, pa7 with blue, green and red curves, respectively, with lighter colours for the runs with 4 times higher spatial resolution) from the *gasLow_fb* (left), *gasHigh_fb* (middle) and *gasHigh_d_fb* (right) simulations at 16 different times in color. The evolution in time is shown with arrows. The 16 different times are equally spaced between $t_{\text{start}} = 25$ Myr and $t_{\text{end}} = 400$ Myr. The circle shown corresponds to t_{end} of the simulation with the corresponding color. Data from Daddi et al. (2010) for the starburst (dashed line) and quiescent (solid line) sequences are over-plotted for reference. For all the simulations, independently of the gas fraction, the simulations with external pressure lie closer to the starburst sequence than the no-pressure simulations. This shows that our toy model for AGN-induced star-formation might be a possible explanation for explaining the increased number of starburst galaxies observed in the distant Universe.

dark red dashed curve is plotted to guide the eye in Fig. 11 representing a square root fit of the SFR as a function of the external pressure applied on the galaxy. One sees that, for the gas-rich *gasHigh* and *gasHigh_d* simulations, the SFR follows the square root of the external pressure very well. At later times, the square root law is only fulfilled until the optimal pressure is reached. For the *gasLow* simulations, the SFR does not scale well with the square root of the external pressure. But as explained above, this was not unexpected.

The bright red points in Fig. 11 are the corresponding points from the *highRes* run. As can be seen in Appendix C the formation of stars in the *highRes* run shows a delay compared to the *lowRes* run. This is due to the increase in star formation threshold for the higher resolution run. Because of this delay, one can also see a delayed behaviour of the SFR of the *highRes* run in Fig. 11. However, at later times, the *highRes* simulation shows a similar behaviour to the *lowRes* simulation.

3.7 The Kennicutt-Schmidt Relation

The Kennicutt-Schmidt (KS) law (Kennicutt 1998) law relates the SFR per unit area as a power of the surface density of gas. This relation holds over several orders of magnitude in both quantities (Krumholz, Dekel, & McKee 2012, and references therein), with the same normalisation for global galaxies (including high redshift ones, Genzel et al. 2010) and giant molecular clouds in the Milky Way (Heiderman et al. 2010; Lada, Lombardi, & Alves 2010) and in the nearby M51 galaxy (Kennicutt et al. 2007). This demonstrates the remarkable universality of the SFR. At high redshift, starburst galaxies lie above the KS law for normal galaxies (Genzel et al. 2010). While the cause of this observed offset is not known, one may speculate that this increased SFR may be caused by positive AGN feedback.

To investigate this in further detail, we check whether our pressurised galactic discs follow the KS relation for normal galaxies, or are above it as starbursts are observed to be, or below it. We adapt here an equivalent technique to Powell et al. (2013) and calculate the half-light radius by assigning a luminosity to each star particle dependent on their age and proportional to their mass (Weidner et al. 2004),

$$L(\text{age} < 10 \text{ Myr}) \propto M_{\text{stars}} \quad (10)$$

$$L(\text{age} > 10 \text{ Myr}) \propto M_{\text{stars}} \left(\frac{\text{age}}{10 \text{ Myr}} \right)^{-0.7} \quad (11)$$

We randomly assign an age in the range 0–5 Gyr for stars that are specified in the initial conditions and therefore have an age equal to zero when the simulation starts. For a given output, Σ_{SFR} is calculated within the half-light radius using the SFR averaged over the previous 10 Myr. The KS relation is calculated by finding the 3D half-light-radius. Within this volume, all the gas above a threshold of 0.1 H cm^{-3} is used to calculate Σ_{gas} and all the new stars are used to calculate Σ_{SFR} , however the quantities are divided by the area $\pi r_{3\text{D}}^2$.

Fig. 12 shows the KS relation at different times for several simulations for the three cases of *gasLow_fb*, *gasHigh_fb*, and *gasHigh_d_fb* with the observed relation from Daddi et al. (2010) overplotted. One can see that, over the course of 400 Myr, all runs lead to an increase in Σ_{SFR} , by one to two dex, with much smaller variations (less than 0.3 dex) in Σ_{gas} . In particular, the runs with high gas fraction (with or without external pressure) show a decrease in Σ_{gas} . This decrease in gas surface density is related to the

gas mass outflow at late times (Fig. 9) and to the consumption of gas by star formation. For the *gasLow* simulation, the evolution of Σ_{gas} is tied to the evolution of the total baryonic mass within the galaxy shown in Fig. 10. The light blue and green lines in Fig. 12 show the *highRes* simulations for the nP and pa3 set, respectively. One can see that the trends of the *highRes* simulation are very similar to the trends of the *lowRes* simulations, specifically at late times. Especially for the pa3 *highRes* simulation, one can see that higher gas densities are reached due to the higher resolution which allows the gas to collapse even further.

For all the simulations independently of the gas fraction, the simulations with external pressure end up being pushed closer to or further beyond the starburst sequence than the corresponding simulations without external pressure. This trend is not changed for the *highRes* runs. Runs with external pressures leading to higher SFR also have a higher Σ_{SFR} and therefore end up even closer to the starburst sequence. For instance, for the *p_spher* simulations, the pa7 run does not extend as far beyond the observed starburst sequence as the pa3 run, which indeed reaches higher SFR for both the *gasLow_fb* and *gasHigh_fb* simulations (Figs. 6 and 11). This is not as significant for the *gasHigh_d_fb* simulations as they do not experience a decrease of SFR but rather that the SFR stays at a certain level after a certain pressure increase ($\sim \text{pa5}$). We therefore see for this simulation set that the KS relations end in a very similar parameter space.

We conclude that this toy model for AGN-induced overpressurisation plausibly leads to AGN-associated star-forming galaxies having enhanced specific star formation rates, for example as suggested by recent observations, cf. (Zinn et al. 2013; Drouart et al. 2014).

4 CONCLUSIONS

It is a fascinating challenge to understand the extreme star formation rates observed for some high-redshift galaxies, typically with luminous AGN and massive outflows: are these caused by higher contents of molecular gas or by a greater efficiency of star formation relative to this molecular gas content? Is turbulence sufficient to explain the high SFR values, or do we need recourse to a more exotic pathway that enhances star formation rates even more? The latter option is motivated by the increasing evidence for the role of AGN in star formation, and in particular their role in a putative phase of positive feedback that accompanies or even precedes the commonly observed massive, star formation-quenching, outflows stimulated by AGN activity.

Using hydrodynamical simulations of isolated disc galaxies embedded in a hot over-pressurised halo, we have been able to study the response of the galaxy SFR to the forcing exerted by this external gas pressure onto the disc. The pressure enhancement triggers instabilities leading to more fragmentation when compared to the no-pressure simulations (Figs. 2 and 3). The enhanced fragmentation leads to the formation of more clumps (Fig. 4) as well as larger values of SFR (Fig. 6). This hints at a positive effect of the pressurisation of the disc and therefore to positive feedback.

We observe a difference in the behaviour for the different ways in which the pressure is applied. In the simulations where external pressure is continuously applied beyond a certain radius (*p_spher* simulations), we observe an optimal pressure beyond which the number of clumps as well as the SFR is decreased. For the simulations where the pressure is instantaneously applied using a density

threshold (over-pressure applied closer to the galaxy disc), such an optimal pressure is not observed.

We have seen that the mass outflow plays a role in explaining this optimal pressure. In particular, for the *gasHigh_fb* simulations, a significant amount of gas gets expelled out of the galaxy, leaving little gas left to form stars and thereby lowering the SFR. The difference in SFR between the high and low external pressures for the *gasLow_fb* simulations is explained by the stagnation of the accumulation of mass in the clumps, which is again related to the large amount of gas that is removed by the incoming pressure wave. Our simulations have been tested with respect to the resolution and local presence or absence of SN explosions: the over-pressurisation of the disc still leads to a positive feedback effect (enhanced SFR).

We found that at given times of the *p_spher* simulations, the SFR (and its mean growth rate) vary as the square root of the applied pressure. We explain this by adapting the Schmidt law for the SFR as a function of 3D gas density for the inclusion of extra pressure caused by the AGN bow shock-driven radio lobe or wind, leading to compression times typically an order of magnitude shorter than the dynamical time, as argued by [Silk & Norman \(2009\)](#).

Though our setup of the extra pressure exerted by circumgalactic gas onto the galaxy is crudely modeled to mimic the pressure confinement by AGN activity, we are confident that such a mechanism could operate in more realistic configurations (see the jet simulations of [Gaibler et al. 2012](#)). We have demonstrated that such pressure confinement of the ISM drives the galaxy into an intense star formation regime, and could explain observations of star formation-enhanced galaxies in the presence of jet activity ([Zinn et al. 2013](#)). Cosmological simulations of pure AGN jet feedback in galaxy clusters ([Dubois et al. 2010](#)) have shown that it has a negative impact on the galaxy SFR on the long-term, though these simulations were lacking spatial resolution in order to properly capture the small-scale fragmentation of the ISM. Our more global picture could suggest a two-stage mechanism for AGN feedback: a compression phase leading to a short burst of star formation, together with the expulsion or heating of the circumgalactic gas leading to a suppression of the gas accretion onto the galaxy and its star formation on longer time-scales. This remains to be verified with simulations of galaxies embedded in a cosmological environment with high spatial resolution and a self-consistent treatment of AGN feedback. We defer this study to future work.

ACKNOWLEDGMENTS

YD and JS acknowledge support by ERC project 267117 (DARK) hosted by UPMC – Sorbonne Universités and JS for support at JHU by National Science Foundation grant OIA-1124403 and by the Templeton Foundation. RB has been supported in part by the Balzan foundation and the Institute Lagrange de Paris. This work has been partially supported by grant Spin(e) ANR-13-BS05-0005 of the French ANR. The simulations have made use of the Horizon cluster. We specially thank S. Rouberol for technical support with the horizon cluster at IAP. We also thank M. D. Lehnert, M. Volonteri, A. Wagner, and J. Coles for valuable discussions.

REFERENCES

Antonuccio-Delogu V., Silk J., 2008, MNRAS, 389, 1750
 Antonuccio-Delogu V., Silk J., 2010, MNRAS, 405, 1303
 Balmaverde B., Baldi R. D., Capetti A., 2008, A&A, 486, 119

Begelman M. C., Cioffi D. F., 1989, ApJ, 345, L21
 Bicknell G. V., Sutherland R. S., van Breugel W. J. M., Dopita M. A., Dey A., Miley G. K., 2000, ApJ, 540, 678
 Bieri R., Dubois Y., Silk J., Mamon G. A., 2015, ApJ, submitted, arXiv:1503.05823
 Bîrzan L., Rafferty D. A., McNamara B. R., Wise M. W., Nulsen P. E. J., 2004, ApJ, 607, 800
 Bleuler A., Teyssier R., 2014, MNRAS, 445, 4015
 Blitz L., Rosolowsky E., 2006, ApJ, 650, 933
 Booth C. M., Schaye J., 2009, MNRAS, 398, 53
 Bower R. G., Benson A. J., Malbon R., Helly J. C., Frenk C. S., Baugh C. M., Cole S., Lacey C. G., 2006, MNRAS, 370, 645
 Churazov E., Sazonov S., Sunyaev R., Forman W., Jones C., Böhringer H., 2005, MNRAS, 363, L91
 Cresci G. et al., 2015, ApJ, 799, 82
 Croft S. et al., 2006, ApJ, 647, 1040
 Croton D. J. et al., 2006, MNRAS, 365, 11
 Daddi E. et al., 2010, ApJ, 714, L118
 Dey A., van Breugel W., Vacca W. D., Antonucci R., 1997, ApJ, 490, 698
 Di Matteo T., Colberg J., Springel V., Hernquist L., Sijacki D., 2008, ApJ, 676, 33
 Di Matteo T., Springel V., Hernquist L., 2005, Nature, 433, 604
 Drouart G. et al., 2014, A&A, 566, A53
 Dubois Y., Devriendt J., Slyz A., Teyssier R., 2010, MNRAS, 409, 985
 Dubois Y., Volonteri M., Silk J., Devriendt J., Slyz A., Teyssier R., 2015, ArXiv e-prints, mNRAS, submitted, arXiv:1504.00018
 Dugan Z., Bryan S., Gaibler V., Silk J., Haas M., 2014, ApJ, 796, 113
 Dunn R. J. H., Fabian A. C., Taylor G. B., 2005, MNRAS, 364, 1343
 Dye S. et al., 2015, ArXiv e-prints
 Elmegreen B. G., 1997, in Revista Mexicana de Astronomia y Astrofisica, vol. 27, Vol. 6, Revista Mexicana de Astronomia y Astrofisica Conference Series, Franco J., Terlevich R., Serrano A., eds., p. 165
 Finkelstein S. L. et al., 2015, ArXiv e-prints, apJ, submitted, arXiv:1504.00005
 Gaibler V., Khochfar S., Krause M., Silk J., 2012, MNRAS, 425, 438
 Genzel R. et al., 2010, MNRAS, 407, 2091
 Heiderman A., Evans, II N. J., Allen L. E., Huard T., Heyer M., 2010, ApJ, 723, 1019
 Hennebelle P., Chabrier G., 2011, ApJ, 743, L29
 Hernquist L., 1990, ApJ, 356, 359
 Hopkins P. F., Narayanan D., Murray N., 2013, MNRAS, 432, 2647
 Hu J., 2008, MNRAS, 386, 2242
 Inskip K. J., Villar-Martín M., Tadhunter C. N., Morganti R., Holt J., Dicken D., 2008, MNRAS, 386, 1797
 Ishibashi W., Fabian A. C., 2012, MNRAS, 427, 2998
 Kainulainen J., Beuther H., Henning T., Plume R., 2009, A&A, 508, L35
 Kennicutt, Jr. R. C., 1998, ApJ, 498, 541
 Kennicutt, Jr. R. C. et al., 2007, ApJ, 671, 333
 Keto E., Ho L. C., Lo K.-Y., 2005, ApJ, 635, 1062
 King A., 2003, ApJ, 596, L27
 Klamer I. J., Ekers R. D., Sadler E. M., Hunstead R. W., 2004, ApJ, 612, L97
 Kormendy J., Bender R., Cornell M. E., 2011, Nature, 469, 374
 Kritsuk A. G., Norman M. L., Wagner R., 2011, ApJ, 727, L20
 Kruijssen J. M. D., Longmore S. N., Elmegreen B. G., Murray N., Bally J., Testi L., Kennicutt R. C., 2014, MNRAS, 440, 3370
 Krumholz M. R., Dekel A., McKee C. F., 2012, ApJ, 745, 69
 Lada C. J., Lombardi M., Alves J. F., 2010, ApJ, 724, 687
 Leroy A. K. et al., 2015, ApJ, 801, 25
 Lombardi M., Lada C. J., Alves J., 2010, A&A, 512, A67
 Magorrian J. et al., 1998, AJ, 115, 2285
 McCarthy P. J., 1993, ARA&A, 31, 639
 McCarthy P. J., van Breugel W., Kapahi V. K., 1991, ApJ, 371, 478
 Navarro J. F., Frenk C. S., White S. D. M., 1997, ApJ, 490, 493
 Padoan P., Nordlund Å., 2011, ApJ, 741, L22
 Podigachoski P. et al., 2015, A&A, 575, A80
 Powell L. C., Bournaud F., Chapon D., Teyssier R., 2013, MNRAS, 434, 1028

Rasera Y., Teyssier R., 2006, *A&A*, 445, 1
Rauch M., Becker G. D., Haehnelt M. G., Carswell R. F., Gauthier J.-R., 2013, *MNRAS*, 431, L68
Rees M. J., 1989, *MNRAS*, 239, 1P
Rosolowsky E., Blitz L., 2005, *ApJ*, 623, 826
Russell H. R., McNamara B. R., Edge A. C., Hogan M. T., Main R. A., Vantyghem A. N., 2013, *MNRAS*, 432, 530
Salomé Q., Salomé P., Combes F., 2015, *A&A*, 574, A34
Sijacki D., Springel V., Di Matteo T., Hernquist L., 2007, *MNRAS*, 380, 877
Silk J., 1997, *ApJ*, 481, 703
Silk J., 2001, *MNRAS*, 324, 313
Silk J., 2005, *MNRAS*, 364, 1337
Silk J., 2013, *ApJ*, 772, 112
Silk J., Norman C., 2009, *ApJ*, 700, 262
Silk J., Rees M. J., 1998, *A&A*, 331, L1
Slyz A. D., Devriendt J. E. G., Bryan G., Silk J., 2005, *MNRAS*, 356, 737
Springel V., Hernquist L., 2005, *ApJ*, 622, L9
Stinson G., Seth A., Katz N., Wadsley J., Governato F., Quinn T., 2006, *MNRAS*, 373, 1074
Sutherland R. S., Bicknell G. V., 2007, *ApJS*, 173, 37
Sutherland R. S., Dopita M. A., 1993, *ApJS*, 88, 253
Swinbank M. et al., 2015, *ArXiv e-prints*
Teyssier R., 2002, *A&A*, 385, 337
Teyssier R., Pontzen A., Dubois Y., Read J. I., 2013, *MNRAS*, 429, 3068
Toro E. F., Spruce M., Speares W., 1994, *Shock Waves*, 4, 25
Tortora C., Antonuccio-Delogu V., Kaviraj S., Silk J., Romeo A. D., Bacciani U., 2009, *MNRAS*, 396, 61
Truelove J. K., Klein R. I., McKee C. F., Holliman, II J. H., Howell L. H., Greenough J. A., 1997, *ApJ*, 489, L179
Turner J. L., Beck S. C., Benford D. J., Consiglio S. M., Ho P. T. P., Kovács A., Meier D. S., Zhao J.-H., 2015, *Nature*, 519, 331
Wagner A. Y., Bicknell G. V., 2011, *ApJ*, 728, 29
Weidner C., Kroupa P., Larsen S. S., 2004, *MNRAS*, 350, 1503
Zinn P.-C., Middelberg E., Norris R. P., Dettmar R.-J., 2013, *ApJ*, 774, 66
Zubovas K., Nayakshin S., Sazonov S., Sunyaev R., 2013, *MNRAS*, 431, 793
Zubovas K., Sabulis K., Naujalis R., 2014, *MNRAS*, 442, 2837

APPENDIX A: BIPOLAR PRESSURE INCREASE

To study the assumption of an isotropic pressure increase, we have performed a simulation of a non-isotropic bipolar pressure increase. For this the pressure has only been increased after a certain height (1.5 kpc) in the vertical direction of the galaxy, where the pressure has been kept at the normal value in the radial direction. The SFR of the *bipolar* and *isotropic* simulations are shown in Fig. A1. One can see that while the *bipolar* SFR oscillates more the general behaviour is not changed by the way pressure is applied on the galaxy.

APPENDIX B: EFFECTS OF SUPERNOVA FEEDBACK

Here, we compare the feedback run with the no-feedback run. In Fig. B1 the gas density maps of the no-pressure enhancement simulations are shown for the non-feedback (nf, left panel) and feedback (fb, right panel) simulations. In Fig. B2 the comparison between fb and nf is shown for the pa3 simulations. We see that for the no-pressure simulations, the effect of SN explosions is to disrupt the interstellar medium into smaller but more numerous clumps. In the edge-on-view, we can also see that the feedback simulation thickens the disc and enhances the mass outflow close to the galaxy. For the pressure simulation, no significant difference can be observed. It shows that the effect of external pressure is stronger than the effect of SN explosions.

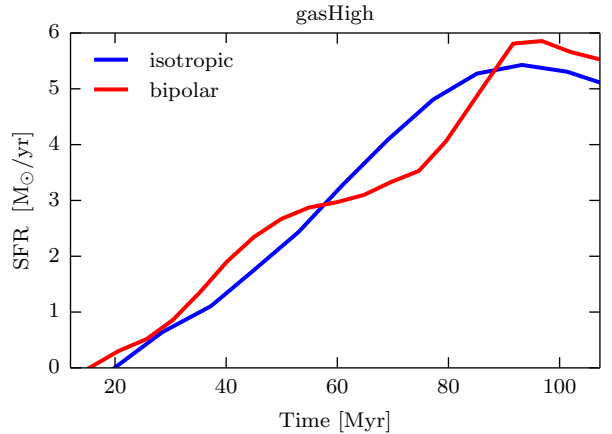


Figure A1. Star formation rate (SFR) as a function of time: In blue for the case where the pressure is applied isotropically (*isotropic*) and in red when the pressure is applied to the galaxy in a bipolar geometry (*bipolar*).

In Fig. B3, we show the number of clumps as a function of time for a selection of the *gasLow* (left), *gasHigh* (middle), and *gasHigh-d* (right) simulations with (fb) or without (nf) SN feedback. In Fig. B4, we show the time evolution of the SFR for the same selection of runs. We see that the number of clumps is enhanced by the presence of SN explosions in all cases since the clumps are regularly destroyed by the SN activity (Dubois et al. 2015). SNe regulate the mass growth of the gas clumps, and since the most massive clumps are expected to capture the smaller clumps, SNe allow for the increase in the number of clumps, thereby reducing their average cross section and mass (see Fig. 7). We also see that the SFR is higher for the non-feedback simulation compared to the feedback simulations as a consequence of the absence of a local regulating process within gas clumps.

Reassuringly, the effect of over-pressurisation of the disc onto the SFR enhancement is independent of the presence of SN explosions: it still leads to a positive feedback effect that SNe only marginally modulate.

APPENDIX C: CONVERGENCE STUDIES

In this section, we test how the results depend on the resolution of the simulation. We performed two high resolution (*highRes*) simulations for the *gasHigh* case, one with no external pressure (nP_hR) and the other with external pressure (pa3_hR). The higher resolution runs have been performed with a resolution of $\Delta x = 10$ kpc (compared to 40 kpc for the standard runs). We changed the density threshold for star formation ($n_0 = 224 \text{ H cm}^{-3}$) in the polytropic EoS as well as the dissipation time-scale of the non-thermal component for the SN feedback ($\Delta x = 10 \text{ pc}$) with the resolution. The simulations were run for a similar timescale (~ 400 Myr) as the lower resolution (*lowRes*) simulations.

In Fig. C1, we show the comparison between the *highRes* and *lowRes* simulations. In the upper panel, the number of clumps is shown for the high and low resolution runs where for both simulations the same clump detection density threshold of 21 H cm^{-3} and a peak-to-saddle threshold of 1.5 was chosen.

Fig. C1 shows that, in both *highRes* and *lowRes* runs, clumps are formed at a faster rate when over-pressure is applied on the

galaxy. Comparing the two resolution runs, we see that the rates of clump formation for both resolutions are comparable at the start of the simulations, for both the pressure and no-pressure runs. While the *lowRes* run with external pressure (pa3) sees a sharp rise in its clump number at 25 Myr, the number of clumps in the *highRes* run with external pressure (pa3_hR) starts catching up after 50 Myr and soon (at 70 Myr) overtakes that of the pa3 run, to end up with nearly double the number of clumps. A similar effect is seen in the no-pressure runs: the number of clumps in the *highRes* simulation starts slowly, but overtakes that of the *lowRes* run (at 230 Myr) to also end up with nearly double the number of clumps.

Similar trends are seen in the star formation histories (lower panel of Fig. C1). For the no-pressure runs, the *highRes* one overtakes the other one in SFR at 280 Myr to end up with twice the SFR, while in the corresponding runs with external pressure, the *highRes* one has its SFR overtake that of the *lowRes* analog at 150 Myr, end the *highRes* run ends up with over double the SFR of the

lowRes one. The very slow rise of the SFRs in the *highRes* runs is the consequence of our choice of a higher density threshold for the *highRes* simulations, which is reached at later times. Once stars start to form, the SFR is greater in the pressure simulation than in the no-pressure simulation. The general effect that the pressurisation leads to more star formation is therefore still the same.

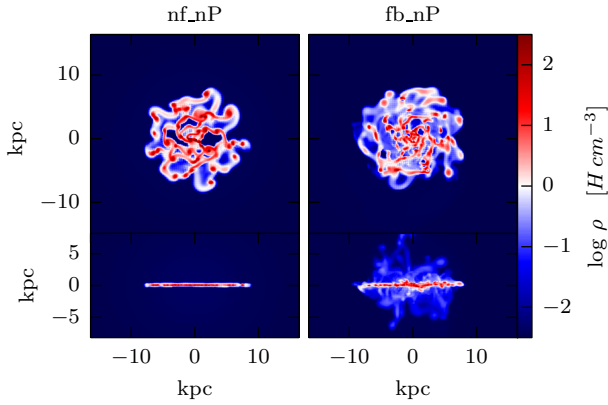


Figure B1. Gas density maps (mass-weighted) of the *gasHigh* non-feedback (left) and feedback (right) simulations without enhancement of the external pressure (nP). The maps are taken at the end of the simulation (~ 400 Myr). Each panel shows both face-on (40×40 kpc, upper part) and edge-on (40×20 kpc, lower part) views.

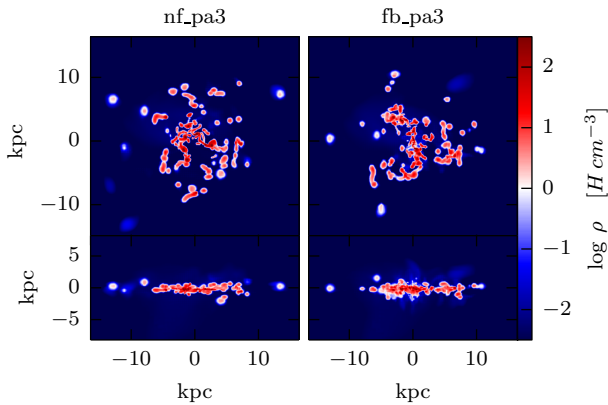


Figure B2. Similar as Fig. B1 but for the simulations with pressure enhancement pa3.

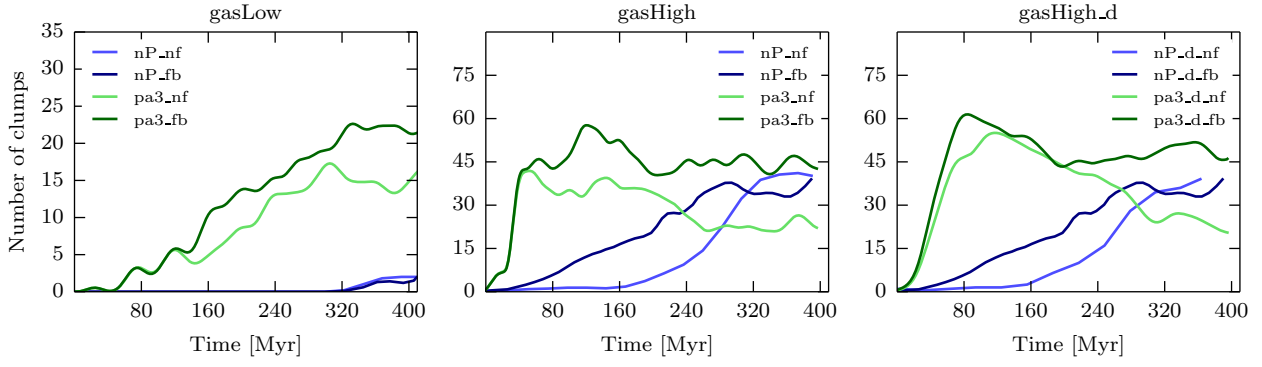


Figure B3. Time evolution of the number of clumps for a selection of the *gasLow* (left), *gasHigh* (middle), and *gasHigh_d* (right) *gasHigh* simulations. For each simulation set the feedback (fb) and non-feedback (nf) runs are shown for comparison. They are indicated by the suffixes in the legend. The lines are smoothed as in Figure 4.

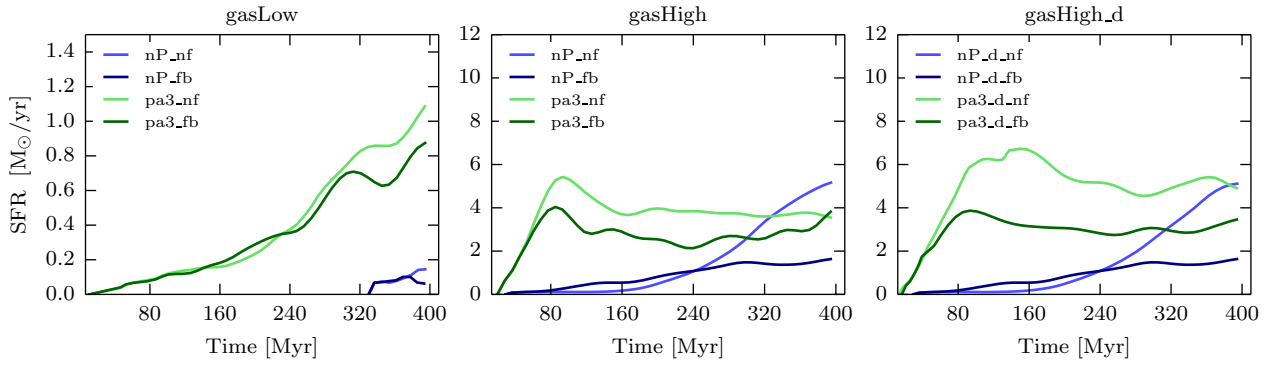


Figure B4. Time evolution of SFR for a selection of the *gasLow* (left), *gasHigh* (middle), and *gasHigh_d* (right) simulations. For each simulation set the feedback (fb) and non-feedback (nf) runs are shown for comparison. They are indicated by suffixes in the legend. The lines are smoothed as in Figure 4.

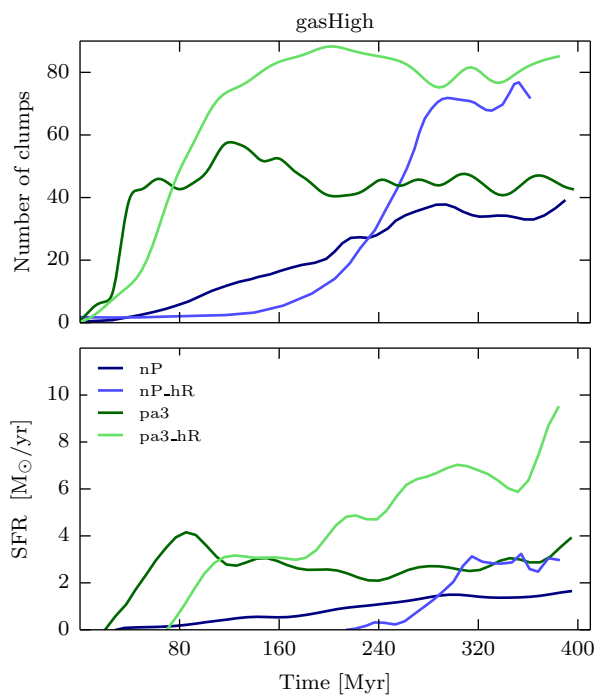


Figure C1. Time evolution of the number of clumps (upper panel) and SFR (lower panel) for the low resolution and high resolution *gasHigh_fb* simulations. The clumps were extracted using a gas density threshold of 21 H cm^{-3} .